

Analyzing power in elastic scattering of ${}^6\text{He}$ from polarized proton target at 71 MeV/nucleon

S. Sakaguchi,^{1,*} Y. Iseri,² T. Uesaka,¹ M. Tanifuji,³ K. Amos,⁴ N. Aoi,⁵ Y. Hashimoto,⁶ E. Hiyama,⁵ M. Ichikawa,⁷ Y. Ichikawa,⁸ S. Ishikawa,³ K. Itoh,⁹ M. Itoh,⁷ H. Iwasaki,⁸ S. Karataglidis,¹⁰ T. Kawabata,¹ T. Kawahara,¹¹ H. Kuboki,⁸ Y. Maeda,¹ R. Matsuo,⁷ T. Nakao,⁸ H. Okamura,^{12,†} H. Sakai,⁸ Y. Sasamoto,¹ M. Sasano,⁸ Y. Satou,⁶ K. Sekiguchi,⁵ M. Shinohara,⁶ K. Suda,¹ D. Suzuki,⁸ Y. Takahashi,⁸ A. Tamii,¹² T. Wakui,⁷ K. Yako,⁸ M. Yamaguchi,¹³ and Y. Yamamoto¹⁴

¹Center for Nuclear Study, University of Tokyo, Tokyo 113-0001, Japan

²Chiba-Keizai College, Chiba 263-0021, Japan

³Science Research Center, Hosei University, Tokyo 102-8160, Japan

⁴School of Physics, University of Melbourne, Melbourne, Australia

⁵RIKEN Nishina Center, Saitama 351-0198, Japan

⁶Department of Physics, Tokyo Institute of Technology, Tokyo 152-8551, Japan

⁷Cyclotron & Radioisotope Center, Tohoku University, Miyagi 980-8578, Japan

⁸Department of Physics, University of Tokyo, Tokyo 113-0033, Japan

⁹Department of Physics, Saitama University, Saitama 338-8570, Japan

¹⁰Department of Physics, University of Johannesburg,

P.O. box 924, Auckland Park, 2006 South Africa

¹¹Department of Physics, Toho University, Chiba, Japan

¹²Research Center for Nuclear Physics, Osaka University, Osaka 567-0047, Japan

¹³Graduate School of Medicine, Gunma University, Gunma 229-8510, Japan

¹⁴Tsuru University, Yamanashi 402-8555, Japan

(Dated: November 5, 2018)

The vector analyzing power has been measured for the elastic scattering of neutron-rich ${}^6\text{He}$ from polarized protons at 71 MeV/nucleon making use of a newly constructed solid polarized proton target operated in a low magnetic field and at high temperature. Two approaches based on local one-body potentials were applied to investigate the spin-orbit interaction between a proton and a ${}^6\text{He}$ nucleus. An optical model analysis revealed that the spin-orbit potential for ${}^6\text{He}$ is characterized by a shallow and long-ranged shape compared with the global systematics of stable nuclei. A semi-microscopic analysis with a $\alpha+n+n$ cluster folding model suggests that the interaction between a proton and the α core is essentially important in describing the $p+{}^6\text{He}$ elastic scattering. The data are also compared with fully microscopic analyses using non-local optical potentials based on nucleon-nucleon g -matrices.

PACS numbers: 24.10.Ht, 24.70.+s, 25.40.Cm, 25.60.Bx, 29.25.Pj

I. INTRODUCTION

Spin-orbit coupling in atomic nuclei is an essential feature in understanding any reaction and nuclear structure related to it. One of the direct manifestations of that spin-orbit coupling in nuclear reactions, is the polarization phenomenon in nucleon elastic scattering [1–3]. Characteristics of the spin-orbit coupling between a nucleon and stable nuclei have been well established by analyses of measured vector analyzing powers in the elastic scattering of polarized nucleons on various targets over a wide range of incident energies [4–7].

On the other hand, the spin-orbit coupling of a nucleon with unstable nuclei might be considerably different from that with the stable nuclei. Some neutron-rich

nuclei with small binding energies are known to have very extended neutron distributions [8]. Since the spin-orbit coupling is essentially a surface effect, it is natural to expect that the diffused density distribution of a neutron-rich nucleus may significantly effect the radial shape and depth of the spin-orbit potential. The purpose of this work is to investigate the characteristics of the spin-orbit potential between a proton and ${}^6\text{He}$; a typical neutron-rich nucleus.

Experimental determination of the spin-orbit potential strongly owes to measurements and analyses of the vector analyzing powers. However, until recently, analyzing power data were not obtained in the scattering which involves unstable nuclei. This was mainly due to the lack of a polarized proton target that is applicable to radioactive ion (RI) beam experiments. RI-beam experiments induced by light ions are usually carried out under inverse-kinematics conditions, where energies of recoil protons can be as low as 10 MeV. Conventional polarized proton targets [9, 10], based on the dynamic nuclear polarization method, require a high magnetic field and low

*Present address: Department of Physics, Kyushu University, Fukuoka 812-8581, Japan;

Electronic address: sakaguchi@phys.kyushu-u.ac.jp

†Deceased.

temperature such as 2.5 T and 0.5 K, respectively. It is impossible to detect the low-energy recoil protons with sufficient angular resolution under these extreme conditions. For the application in RI-beam experiments, we have constructed a solid polarized proton target which can be operated under low magnetic field of 0.1 T and at high temperature of 100 K [11–15]. The electron polarization in photo-excited aromatic molecules is used to polarize the protons [16, 17]. A high proton polarization of about 20% can be achieved in relatively “relaxed” operating conditions described above, since the magnitude of the electron polarization is almost independent of the magnetic field strength and temperature.

We have measured the vector analyzing power for the $p+{}^6\text{He}$ elastic scattering at 71 MeV/nucleon [18] using the solid polarized proton target, newly constructed for RI-beam experiments. ${}^6\text{He}$ is suitable for the present study since it has a spatially extended distribution due to a small binding energy. In addition, from an experimental viewpoint, the $p+{}^6\text{He}$ elastic scattering measurement is relatively easy to perform since ${}^6\text{He}$ does not have a bound excited state. This allows us to identify the elastic-scattering event only by detecting ${}^6\text{He}$ and a proton in coincidence. The analyzing powers thus measured are the first data set that can be used for quantitative evaluation of the spin-orbit interaction between a proton and an unstable ${}^6\text{He}$ nucleus. The essence of these measurements has been published in Ref. [18] together with two kinds of theoretical analyses by folding models; one assumes a fully antisymmetrized large-basis shell model for ${}^6\text{He}$ with the g -matrix interaction and the other an $\alpha+n+n$ cluster model for ${}^6\text{He}$ with a p - n effective interaction and a realistic p - α static potential. The main purpose of the present paper is to give more details of the experiment and present an additional analysis of the experimental data using a one-body p - ${}^6\text{He}$ optical potential. The analysis exhibits remarkable characteristics for the spin-orbit part of that potential. Then it becomes important to investigate if such a potential can be derived theoretically from any model of ${}^6\text{He}$. As the first approach we examined the $\alpha+n+n$ folding potential in more detail, since important contributions of the α cluster are suggested by the fact that the measured A_y for ${}^6\text{He}$ is similar to that for ${}^4\text{He}$ [18], when plotted versus the momentum transfer of the scattering. To identify effects of the clusterization, we also calculated the p - ${}^6\text{He}$ folding potential for a $2p+4n$ non-cluster model of ${}^6\text{He}$ and compared the results with those of the $\alpha+n+n$ cluster model. Hereafter, they are referred to as the ann cluster folding (CF) model and nucleon folding (NF) one, respectively. In addition, the data are also compared with fully microscopic calculations using non-local optical potentials. In this model, non-locality of the p - ${}^6\text{He}$ interaction, a consequence of the Pauli principle leading to nucleon exchange scattering amplitudes, is taken into account explicitly. Three sets of single-particle wave functions, as well as the required one-body density matrix elements determined from a large-basis shell model for ${}^6\text{He}$, have

been used in these calculations.

The present paper is subdivided as follows. In Section 2, details of the experimental method are described. In Section 3, the method of the data reduction is presented. Section 4 deals with the phenomenological optical model analysis. Section 5 is devoted to the details of the ann cluster folding calculation and the nucleon folding calculation. In Section 6, the data are compared with the analysis by the non-local g -folding optical potentials. Finally, a short summary of the obtained results is given in Section 7.

II. EXPERIMENT

A. Experimental setup

The experiment was carried out at the RIKEN Accelerator Research Facility (RARF). The ${}^6\text{He}$ beam was produced through the projectile fragmentation of a ${}^{12}\text{C}$ beam with an energy of 92 MeV/nucleon bombarding a primary target. As that primary, we used a rotating ${}^9\text{Be}$ target [19] to avoid heat damage by the beam. A thickness of the target was 1480 mg/cm². The ${}^6\text{He}$ particles were separated by the RIKEN Projectile-fragment Separator (RIPS) [20] based on the magnetic rigidity and the energy loss of fragments. The energy of the ${}^6\text{He}$ beam was 70.6 ± 1.4 MeV/nucleon at the center of the secondary target. The purity of the beam was 95%.

The solid polarized proton target was placed at the final focal plane of RIPS. Figure 1 illustrates the experimental setup of the target and detectors. The most prominent advantage of the target is its relaxed operating conditions, i.e. a low magnetic field of 0.1 T and high temperature of 100 K. These conditions allow us to detect recoil protons whose energies are as low as 10 MeV. Details of the target will be described in the following subsection.

A detector system consisted of two subsystems: one for scattered particles and the other for recoil protons. Detection of the recoil protons with energies as low as 10 MeV is essential for the selection of the elastic-scattering events. The scattering angles of protons were determined by single-wire drift chambers (SWDC). The SWDCs were placed 138.5 mm away from the target on both left and right sides of the beam axis as shown in Fig. 1. They covered an angular region of 39° – 71° (horizontal) and $\pm 9.7^\circ$ (vertical) in the laboratory system. Their position resolution and detection efficiency were found to be 2.6 mm (FWHM) and 99.3%. For the measurement of the total energy of protons, we used CsI(Tl) scintillation detectors. They were placed just behind the SWDCs. Light output from the CsI(Tl) crystal was detected by photo-multiplier tubes. The front side of the CsI(Tl) scintillator was covered by the thin carbon-aramid film with a thickness of 12 μm . Material thickness of the film, the SWDC, and air between the detectors was 24 mg/cm² in total. Energy loss of 10 MeV protons in

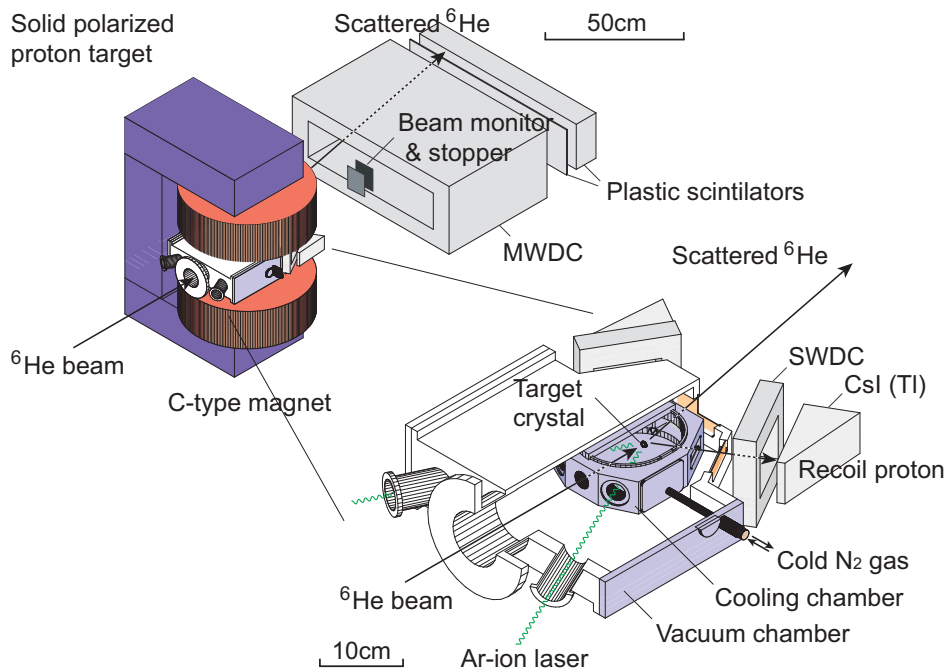


FIG. 1: (Color online) Experimental setup of the secondary target and detectors is shown.

these materials is 1.2 MeV, which does not prevent the detection.

A multi-wire drift chamber (MWDC) was used to reconstruct the trajectories of scattered particles. Scattering position on the secondary target was determined from the reconstructed trajectory. The MWDC was placed at 880 mm downstream of the target. It has a sensitive area of 640 mm (horizontal) \times 160 mm (vertical) and covered an angular region of $\pm 16^\circ \times \pm 4^\circ$ in the laboratory system. The configuration of the planes of the MWDC is X-Y-X'-Y'-X'-Y'-X-Y, where “X(Y)-plane” has anode-wires oriented along the vertical (horizontal) axis. The planes with primes are displaced with respect to the “unprimed” planes by half the cell size. The cell size is 20 mm \times 20 mm for the X-plane and 10 mm \times 10 mm for the Y-plane. The material of the anode wire is gold-plated tungsten with a diameter of 30 μ m. Negative high voltages were applied to the cathode and potential wires: -2.85 kV for the X (X')-planes and -2.15 kV for the Y (Y')-planes. A gas mixture of Ar (50%) and C₂H₆ (50%) was used. Position resolution and detection efficiency of the MWDC were found to be 0.2 mm (FWHM) and 99.8%. For identification of scattered particles, we used a plastic scintillation detector array placed just behind the MWDC. The first and second layers with thicknesses of 5 mm and 100 mm provided information of the energy loss and the total energy of scattered particles. The total number of the beam particles was counted with a beam monitor placed between the secondary target and the MWDC. A 50 mm^H \times 50 mm^V \times 10 mm^D plastic scintillator was used for the beam monitor. A beam stopper made of a copper

block was placed just behind the beam monitor.

B. Solid polarized proton target

The solid polarized proton target, used in the measurement, can be operated in a low magnetic field of 0.1 T and at a high temperature of 100 K. These relaxed operation conditions allow us to detect low-energy recoil protons without losing angular resolution. This capability is indispensable to apply the target to scattering experiments carried out under the inverse kinematics condition. The proton polarization of about 20% has been achieved [15] under such relaxed conditions by introducing a new polarizing method using electron polarization in triplet states of photo-excited aromatic molecules [16, 17]. A single crystal of naphthalene (C₁₀H₈) doped with a small amount of pentacene (C₂₂H₁₄) is used as the target material. Protons in the crystal are polarized by repeating a two-step process: production of electron polarization and polarization transfer. In the first step, pentacene molecules are optically excited to higher singlet states. A small fraction of them decays to the first triplet state via the first excited singlet state by the so-called intersystem crossing. Here, electron population difference is spontaneously produced among Zeeman sublevels of the triplet state [16]. In the second step, the electron population difference between two Zeeman sublevels, namely electron polarization, is transferred to the proton polarization by the cross-relaxation technique [17].

As the target material, we used a single crystal of naph-

thalene doped with 0.005 mol% pentacene molecules. The crystal was shaped into a thin disk whose diameter and thickness are 14 mm and 1 mm (116 mg/cm^2), respectively. The number of hydrogens per unit area was $4.29 \pm 0.13 \times 10^{21} / \text{cm}^2$. In order to reduce the relaxation rate, the target crystal was cooled down to 100 K in a cooling chamber with the flow of cold nitrogen gas. The cooling chamber was installed in another chamber as shown in Fig. 1. Heat influx to the cooling chamber was reduced by the vacuum kept in the intervening space between these two chambers. Each chamber has one window ($6 \text{ }\mu\text{m}$ -thick Havar foil) on the upstream side for the incoming RI-beam, two glass windows for the laser irradiation, and three windows ($20 \text{ }\mu\text{m}$ -thick Kapton foil) on the left, right, and downstream sides for the detection of recoil and scattered particles.

A static magnetic field was applied on the target crystal by a C-type electromagnet to define the polarizing axis. The gap and the diameter of the poles were 100 mm and 220 mm, respectively. The strength of the magnetic field in the present experiment was 91 mT; a value much higher than that of the crystal field ($\approx 2 \text{ mT}$). While the effects of the magnetic field on the scattering angles of ${}^6\text{He}$ particles and protons were sufficiently small (about 0.07° and $0.2\text{--}0.8^\circ$, respectively), they were properly corrected in the data analysis.

The target crystal was irradiated by the light of two Ar-ion lasers with a power of 25 W each in the multiline mode. Wavelengths of main components of the light were 514.5 nm (10 W) and 488.5 nm (8 W). The laser light was pulsed by a rotating optical chopper. Typically the pulse width and repetition rate were 12–14 μs and 1 kHz. Microwave (MW) irradiation and a magnetic field sweep are required in the cross-relaxation method. For the MW irradiation, the target crystal was installed in a resonator. In order to detect low-energy recoil protons, we employed a thin cylindrical loop-gap resonator (LGR [21]) made of 25 μm -thick Teflon film. Copper stripes with a thickness of 4.4 μm were printed on both sides of the film. The MW frequency was 3.40 GHz. The LGR was surrounded by a cylindrical MW shield made of 12 μm -thick aluminum foil. For the cross-relaxation, the magnetic field was swept from 88 mT to 94 mT at the rate of 0.36 mT/ μs , simultaneously with the MW irradiation, by applying a current to a small coil placed in the vicinity of the target material.

Proton polarization was monitored during the experiment by the pulse NMR method. A radio-frequency (RF) pulse with a frequency and a duration of 3.99 MHz and 2.2 μs was applied to a 19 mm ϕ NMR coil covering the target crystal. The free induction decay (FID) signal was detected by the same coil. We carried out the absolute calibration to relate the FID signal to the proton polarization by measuring the spin-asymmetry in the $p+{}^4\text{He}$ elastic scattering. Details of the calibration procedure are described in Appendix. A.

Devices located near to the target, namely the LGR, the MW shield, the field sweeping coil, and the NMR

coil, were fabricated with hydrogen-free materials to prevent production of background events. Table I shows the material thicknesses of the devices that recoil protons penetrate. Energy losses of the 20 MeV protons in these materials are sufficiently small for the detection as summarized in Table I.

The target polarization during the experiment is shown in Fig. 2 as a function of time. The polarization was built up for the first 40 hours and reached the maximum value of $20.4 \pm 3.9\%$. The target was then irradiated by a 71 MeV/nucleon ${}^6\text{He}$ beam for 55 hours, by a 80 MeV/nucleon ${}^4\text{He}$ beam for the following 25 hours, and again by the ${}^6\text{He}$ beam for 60 hours. The magnitude of average polarization was found to be $13.8 \pm 2.7\%$. The target polarization slowly decreased as a function of time, which is due to beam-irradiation damage in the target material. This radiation damage increased the relaxation rate of the target material from $\Gamma = 0.127(6) \text{ h}^{-1}$ before the experiment to $\Gamma = 0.295(4) \text{ h}^{-1}$ after the beam irradiation. The direction of the target polarization was reversed three times during the measurement to cancel spurious asymmetries. The 180° pulse NMR method was used here. Reversal efficiency of 60–70% was achieved.

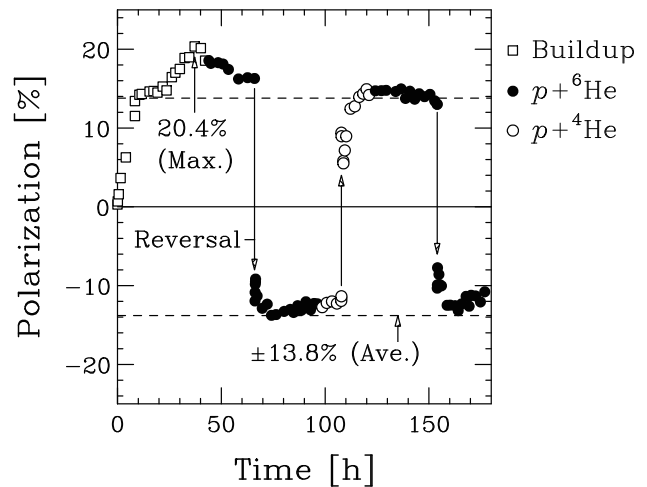


FIG. 2: Target polarization is shown as a function of time. The open squares, closed circles, and open circles indicate the target polarization during the polarization buildup, the $p+{}^6\text{He}$ elastic-scattering measurement, and the $p+{}^4\text{He}$ elastic-scattering measurement, respectively.

III. DATA REDUCTION

A. Data analysis

In principle, elastic-scattering events of the ${}^6\text{He}$ from protons can be identified by the coincidence detection of scattered ${}^6\text{He}$ particles and recoil protons, since the ${}^6\text{He}$ does not have a bound excited state. Note that the first excited state of ${}^6\text{He}$, which is the 2^+ state at 1.87 MeV, is

| Material | Thickness (mg/cm ²) | Energy loss (MeV) |
|-------------------------------|---------------------------------|-------------------|
| Target crystal (Naphthalene) | 0 – 336 | 0 – 9.5 |
| LGR (Teflon, Cu foil) | 9.3 | 0.2 – 0.4 |
| Microwave shield (Al foil) | 3.2 | 0.05 – 0.1 |
| Cooling gas (N ₂) | 13.5 | 0.3 – 0.6 |
| Window (Kapton film) | 20 | 0.5 – 1.0 |
| Total | 46 – 382 | 1.1 – 11.6 |

TABLE I: Thicknesses of the materials of target devices and energy losses of 20 MeV recoil protons in them.

above the two-neutron breakup threshold (0.975 MeV). Thus, any excited ${}^6\text{He}$ particles decay into $\alpha+n+n$ systems before reaching the detectors.

Scattered particles were identified by the standard ΔE - E method. Figure 3 shows a two-dimensional plot of the total energies of scattered particles E versus their energy losses ΔE , where loci of tritons, ${}^4\text{He}$, ${}^6\text{He}$, and ${}^8\text{Li}$ are found. Tritons and ${}^8\text{Li}$ are the contamination in the secondary beam. Most of ${}^4\text{He}$ particles were produced by ${}^6\text{He}$ dissociation in the secondary target. However, some originated from ${}^6\text{He}$ reactions in the plastic scintillators. So to count all of the $p+{}^6\text{He}$ elastic-scattering events, the particle identification gate includes most of the ${}^4\text{He}$ locus as shown by solid curves in Fig. 3. The contribution of the dissociation reaction, which is not excluded by this gate, was subtracted using a kinematics relation. This is described after the response of the recoil proton detectors is considered.

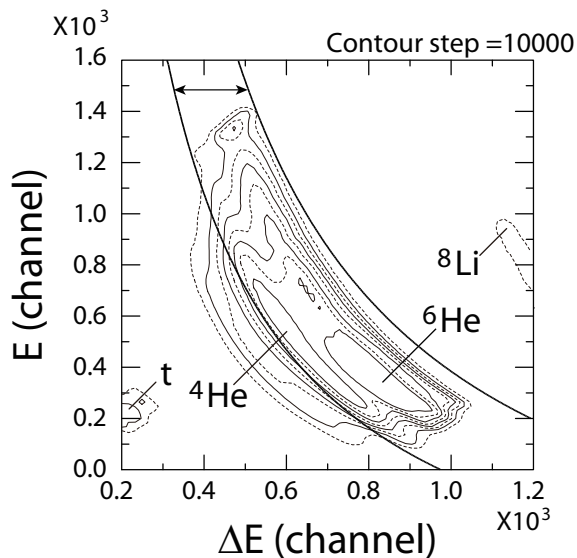


FIG. 3: Two-dimensional plot of the total energies of scattered particles versus their energy losses. Solid curves indicate the particle-identification gate.

Figure 4 shows a two-dimensional scatter plot of the proton energies versus their scattering angles in the center-of-mass system, $\theta_{\text{c.m.}}$. The kinematic locus of the elastic scattering is clearly identified, while backgrounds

from other reaction channels such as $p({}^6\text{He}, p{}^4\text{He})$ are also evident. The kinematic locus of elastic-scattering events shows that the recoil protons were properly detected outside of the target. It should be noted that this correlation was not used for the event selection, since it would cause a loss of the events at forward angles.

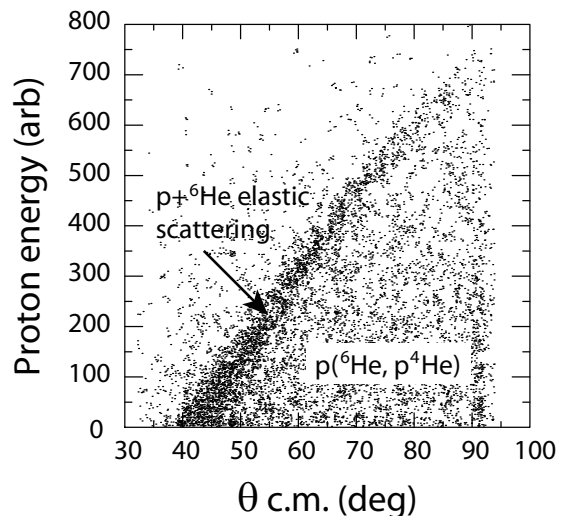


FIG. 4: Two-dimensional plot of the proton energies versus their scattering angles.

To discriminate elastic scattering from the background, we used the correlation of the azimuthal angles of protons ϕ_p with those of scattered particles $\phi_{\text{scatt.}}$. In the case of the elastic scattering, a scattered ${}^6\text{He}$ and a recoil proton stay within a well defined reaction plane since the final state is a binary system. Thus, the difference of azimuthal angles $\Delta\phi = \phi_p - \phi_{\text{scatt.}}$ makes a narrow peak at around 180° . This back-to-back correlation holds even if the scattered ${}^6\text{He}$ is dissociated in the plastic scintillator. In the case of other reactions, however, the azimuthal angle difference is more spread since their final states consist of more than two particles.

Figure 5 shows the distribution of the azimuthal angle difference $\Delta\phi$ fitted by a double-Gaussian function. The narrower component is reasonably identified as that of the elastic-scattering events. The peak width of 3.5° in sigma is consistent with the detector resolution of 3.1° . We selected the events of $|\Delta\phi - 180^\circ| < 12.4^\circ$. The

background remaining in the gate was evaluated from the broader component and was subtracted. Contributions of the inelastic scattering and other reactions such as breakup were removed in this way without losing the elastic-scattering yields. Figure 6 shows a background-subtracted two-dimensional plot of scattering angles in the center-of-mass system versus angles of scattered particles. Center-of-mass scattering angles were deduced from recoil angles of the protons in the laboratory system, since the resolution of scattering angles of ${}^6\text{He}$ particles is insufficient due to the kinematic focusing. In Fig. 6, clear peaks of elastic-scattering events lie along the solid curves indicating the kinematics of the $p+{}^6\text{He}$ elastic scattering. Small peaks at $|\theta_{6\text{He}}| \approx 4^\circ$ originated from the ambiguity in the background subtraction. Yields of the $p+{}^6\text{He}$ elastic scattering were obtained by counting the events of the elastic-scattering peaks in the typical width of 4° in $\theta_{6\text{He}}$.

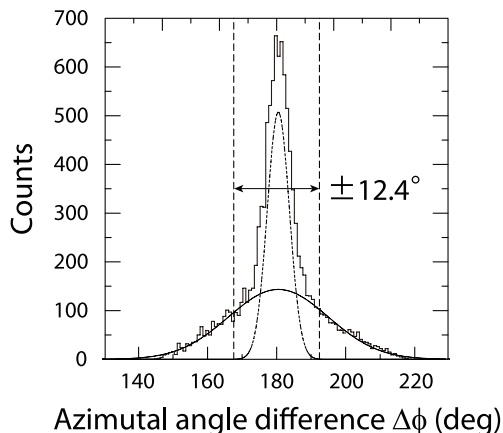


FIG. 5: Azimuthal angle difference between scattered particles and recoil protons, fitted by a double-Gaussian function.

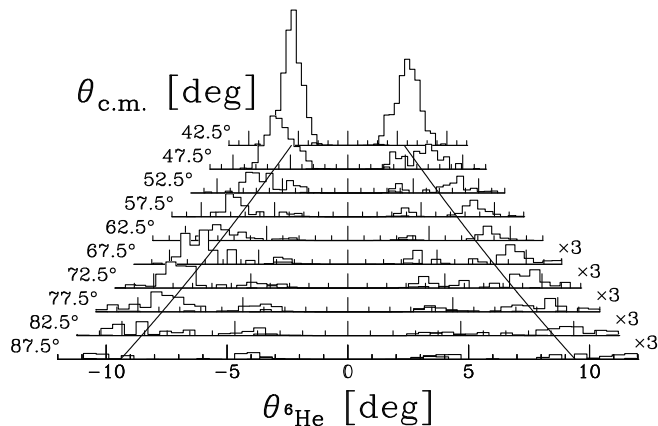


FIG. 6: Scattering angle correlation between scattered particles and recoil protons. The solid curves indicate the kinematics of the $p+{}^6\text{He}$ elastic scattering.

The present work demonstrates the applicability of the solid polarized proton target in the RI-beam experiment. The relaxed operation condition of the target, i.e. a low magnetic field of 0.1 T and high magnetic field of 100 K, enables us to detect the low-energy recoil protons. As described in the data analysis above, information on the trajectory of recoil proton is indispensable both in identifying the elastic-scattering events (Fig. 5) and in deducing the scattering angle (Fig. 6).

B. Experimental data

The $d\sigma/d\Omega$ of the $p+{}^6\text{He}$ elastic scattering measured at 71 MeV/nucleon are summarized in Table II. In the backward region, the uncertainty mainly results from statistics and from the ambiguity in the background subtraction. In the forward angular region, $\theta_{\text{c.m.}} < 60^\circ$, the main component of the uncertainty in $d\sigma/d\Omega$ is the systematic uncertainty in the number of the incident particles (10%). The target was hit by only a fraction of beam particles since the size of the secondary beam was comparable to that of the target. The percentage of the beam particles incident on the target was determined from the beam profile and was found to be $65 \pm 7\%$ of those counted by the beam monitor. The beam profile was measured with the MWDC by removing the beam stopper. Stability of the beam profile was confirmed by several measurements carried out before, during, and after the elastic-scattering measurement.

The analyzing power A_y is deduced with the standard procedure as

$$A_y = \frac{1}{P} \frac{L - R}{L + R}, \quad L = \sqrt{N_L^\uparrow \cdot N_R^\downarrow}, \quad R = \sqrt{N_L^\downarrow \cdot N_R^\uparrow},$$

where P denotes the target polarization. The values N 's represent the yield of the elastic-scattering events where subscripts and superscripts denote the scattering direction (left/right) and the polarization direction (up/down), respectively. The statistical uncertainty is expressed by

$$\frac{\Delta A_y}{A_y} = \frac{LR}{L^2 - R^2} \sqrt{\frac{1}{N_R^\uparrow} + \frac{1}{N_R^\downarrow} + \frac{1}{N_L^\uparrow} + \frac{1}{N_L^\downarrow}}.$$

This procedure allows us to minimize the systematic uncertainties originating from unbalanced detection efficiencies and misalignment of detectors. The obtained A_y are summarized in Table III. It must be noted that there is an additional scale error of 19% resulting from the uncertainty in the target polarization P (see Appendix. A).

Figure 7 shows $d\sigma/d\Omega$ and A_y for the $p+{}^6\text{He}$ elastic scattering at 71 MeV/nucleon (closed circles: present work, open circles: Ref. [22]), those for the $p+{}^4\text{He}$ at 72 MeV/nucleon (open squares: Ref. [23]), and those for the $p+{}^6\text{Li}$ at 72 MeV/nucleon (open triangles: Ref. [24]). The present data are consistent with the previous ones in

| $\theta_{c.m.}$ (deg) | $\Delta\theta_{c.m.}$ (deg) | $\frac{d\sigma}{d\Omega}$ (mb/sr) | $\Delta\frac{d\sigma}{d\Omega}$ (mb/sr) |
|-----------------------|-----------------------------|-----------------------------------|---|
| 42.1 | 2.5 | 5.02 | 0.52 |
| 47.1 | 2.5 | 2.03 | 0.22 |
| 52.1 | 2.5 | 0.796 | 0.098 |
| 57.4 | 2.5 | 0.454 | 0.059 |
| 62.3 | 2.5 | 0.360 | 0.046 |
| 67.3 | 2.5 | 0.226 | 0.031 |
| 72.3 | 2.5 | 0.172 | 0.023 |
| 77.3 | 2.5 | 0.127 | 0.018 |
| 82.2 | 2.5 | 0.064 | 0.013 |
| 87.2 | 2.5 | 0.038 | 0.012 |

TABLE II: Differential cross sections for the $p+{}^6\text{He}$ elastic scattering at 71 MeV/nucleon. The $\Delta\theta_{c.m.}$ denotes the bin width. The $\Delta\frac{d\sigma}{d\Omega}$ denotes the quadratic sum of the statistical and systematic uncertainties.

| $\theta_{c.m.}$ (deg) | $\Delta\theta_{c.m.}$ (deg) | A_y | ΔA_y |
|-----------------------|-----------------------------|--------|--------------|
| 37.1 | 2.5 | 0.242 | 0.069 |
| 44.6 | 5.0 | 0.021 | 0.089 |
| 54.6 | 5.0 | -0.016 | 0.135 |
| 64.8 | 5.0 | 0.11 | 0.18 |
| 74.3 | 5.0 | -0.27 | 0.27 |

TABLE III: Analyzing powers for the $p+{}^6\text{He}$ elastic scattering at 71 MeV/nucleon. ΔA_y denotes the statistical uncertainty. Note that there is an additional scale error of 19% resulting from the uncertainty in the target polarization. The $\Delta\theta_{c.m.}$ denotes the bin width.

Ref. [22] in an overlapping angular region of $\theta_{c.m.} = 40\text{--}50^\circ$. We extended the data to the backward angles of $\theta_{c.m.} \approx 90^\circ$. It is found that the $d\sigma/d\Omega$ of $p+{}^6\text{He}$ are almost identical with those of $p+{}^6\text{Li}$ at $\theta_{c.m.} = 20\text{--}90^\circ$, while they have a steeper angular dependence than those of $p+{}^4\text{He}$. In good contrast to the similarity found in $d\sigma/d\Omega$, A_y data are widely different between $p+{}^6\text{He}$ and $p+{}^6\text{Li}$. The A_y of $p+{}^6\text{Li}$ increase as a function of the scattering angle in an angular region of $\theta_{c.m.} = 40\text{--}70^\circ$ and take large positive values. This behavior is commonly seen in proton elastic scattering from stable nuclei at the present energy region [25]. Unlike this global trend, A_y of $p+{}^6\text{He}$ decreases in $\theta_{c.m.} = 37\text{--}55^\circ$, which is rather similar to those of $p+{}^4\text{He}$. While the large error bars prevent us from observing the difference between A_y of $p+{}^6\text{He}$ and of $p+{}^4\text{He}$, it is clearly seen that the angular distribution of the A_y in $p+{}^6\text{He}$ deviates from that of $p+{}^6\text{Li}$.

IV. PHENOMENOLOGICAL OPTICAL MODEL ANALYSIS

A. Optical potential fitting

The aim of this section is to extract the gross characteristics of the spin-orbit interaction between a proton and

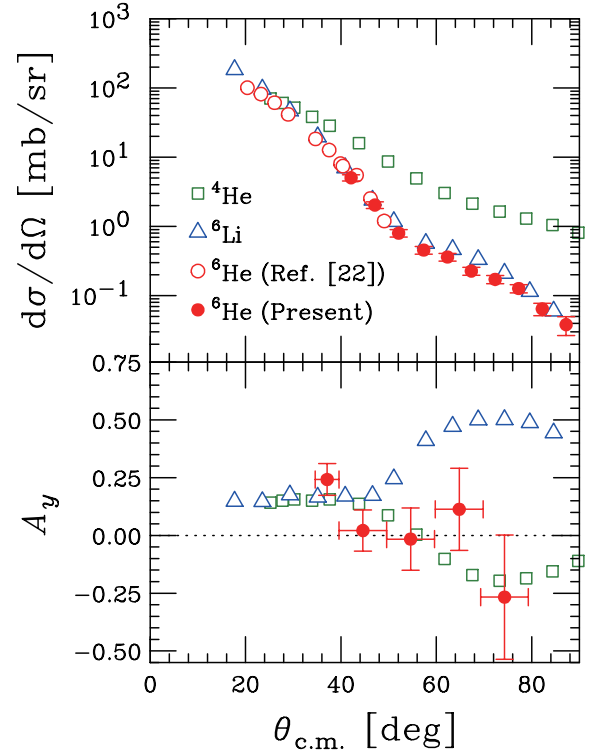


FIG. 7: (Color online) Differential cross sections and analyzing powers of the $p+{}^4\text{He}$ at 72 MeV (open squares: Ref. [23]), of the $p+{}^6\text{Li}$ at 72 MeV (open triangles: Ref. [24]), and of the $p+{}^6\text{He}$ at 71 MeV (open circles: Ref. [22], closed circles: present work).

${}^6\text{He}$. For this purpose, we determined the optical model potential that reproduces the experimental data of both differential cross sections and analyzing powers. The optical model potential obtained in this phenomenological approach will be compared with the semi-microscopic calculations in Section V.

We adopted a standard Woods-Saxon optical potential with a spin-orbit term of the Thomas form:

$$\begin{aligned}
 U_{\text{OM}}(R) = & -V_0 f_r(R) - iW_0 f_i(R) \\
 & + 4i a_{id} W_d \frac{d}{dR} f_{id}(R) \\
 & + V_s \frac{2}{R} \frac{d}{dR} f_s(R) \mathbf{L} \cdot \boldsymbol{\sigma}_p + V_C(R) \quad (1)
 \end{aligned}$$

with

$$\begin{aligned}
 f_x(R) = & \left[1 + \exp\left(\frac{R - r_{0x} A^{1/3}}{a_x}\right) \right]^{-1} \quad (2) \\
 (x = & r, i, id, \text{ or } s).
 \end{aligned}$$

Here, \mathbf{R} is the relative coordinate between a proton and a ${}^6\text{He}$ particle (see Fig. 12 (b)), $\mathbf{L} = \mathbf{R} \times (-i\hbar\nabla_{\mathbf{R}})$ is the associated angular momentum, and $\boldsymbol{\sigma}_p$ is the Pauli spin operator of the proton. The subscripts r , i , id , and s denote real, volume imaginary, surface imaginary, and

spin-orbit, respectively. V_C is the Coulomb potential of uniformly charged sphere with a radius of $r_{0C}A^{1/3}$ fm ($r_{0C} = 1.3$ fm).

The search procedure for the best-fit potential parameters was made in two steps: first the parameters of the central term were found by minimizing the χ^2 values of $d\sigma/d\Omega$, and second the parameters of the spin-orbit term by fitting A_y . These two steps were iterated alternately until convergence was achieved. Such a procedure is feasible since the contribution of the spin-orbit potential to $d\sigma/d\Omega$ is much smaller than those of the central terms. In the fitting, we used the data in Ref. [22] and the present ones. Uncertainties of $d\sigma/d\Omega$ smaller than 10% were artificially set to 10% in order to avoid trapping in an unphysical local χ^2 minimum. The fitting was carried out using the ECIS79 code [26]. A set of parameters for the $p+{}^6\text{Li}$ elastic scattering at 72 MeV/nucleon [24], labeled as Set-A in Table IV, was used as the initial values in the search of the $p+{}^6\text{He}$ potential parameters.

The parameters obtained for the $p+{}^6\text{He}$ elastic scattering are labeled as Set-B in Table IV. The reduced χ^2 values for $d\sigma/d\Omega$ and A_y were 0.95 and 0.96, respectively. Uncertainties of the parameters of the spin-orbit potential, r_{0s} , a_s , and V_s , are evaluated in the following manner. Figure 8 shows the contour map of the deviation of χ^2 value for A_y from that calculated by the Set-B (as indicated by the point-P), $\Delta\chi_{A_y}^2$, on the two-dimensional plane of r_{0s} and a_s after projecting with optimized V_s at each point of the plane. In the figure, a simultaneous confidence region for r_{0s} and a_s is presented by the solid contour indicating $\Delta\chi_{A_y}^2 = 1$. In this region, the optimum V_s ranges between 1.15 MeV (at the point-Q) and 2.82 MeV (at the point-R). In the r_{0s} - a_s - V_s space, a surface that $\Delta\chi_{A_y}^2 = 1$ touches planes that are expressed by $r_{0s} = 1.29 \pm 0.13$ fm, $a_s = 0.76 \pm 0.17$ fm, and $V_s = 2.02 \pm 0.87$ MeV, which gives a rough estimation for uncertainties of the parameters.

B. Characteristics of spin-orbit potential

In Fig. 9, the results of calculations of the observables made with the optical potentials of Set-A, -B, and -C in Table IV are shown together with the experimental data. Set-C was taken from Ref. [27], where a phenomenological optical model potential that reproduced only the previous $d\sigma/d\Omega$ data of the $p+{}^6\text{He}$ at 71 MeV/nucleon [22] was reported. The radial dependences of the $p+{}^6\text{He}$ optical potentials (Set-B and Set-C) are shown in Fig. 10 by solid and dashed lines, respectively.

The calculation with the potential Set-C reasonably reproduces the present $d\sigma/d\Omega$ data, whereas it largely deviates from the A_y data at $\theta_{\text{c.m.}} \gtrsim 40^\circ$. It should be noted that the A_y data were unavailable when the potential Set-C was sought. The calculation with the potential Set-B reproduces both $d\sigma/d\Omega$ and A_y over whole angular region except for the most backward data point of A_y . Similarity of the $d\sigma/d\Omega$ calculated with Set-B and Set-

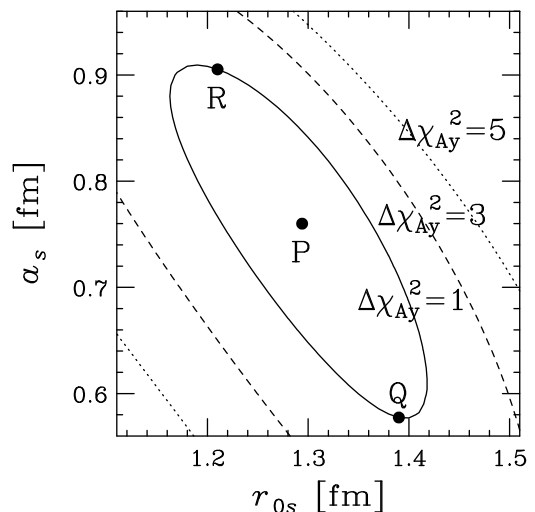


FIG. 8: Contour map of the $\Delta\chi_{A_y}^2$ values (see the text for the definition) on the two-dimensional plane of r_{0s} and a_s . The solid, dashed, and dotted curves indicate $\Delta\chi_{A_y}^2=1$, 3, and 5, respectively. The point that gives the best-fit parameters, Set-B in Table IV, is indicated by the point-P. See the text for the points-Q and -R.

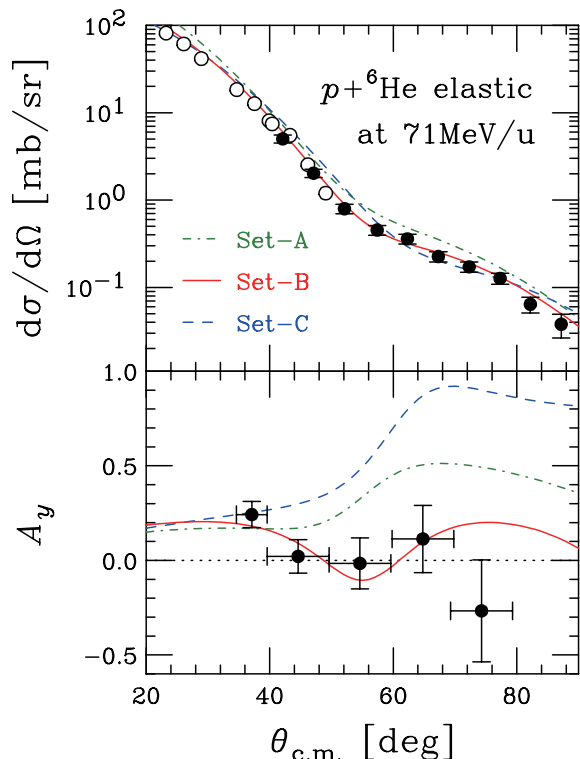


FIG. 9: (Color online) Differential cross sections and analyzing powers calculated by the phenomenological optical potentials are shown together with the experimental data. The dot-dashed curves denote calculations of the Set-A in Table IV, the solid curves those of set-B, and the dashed curves those of Set-C. Solid circles are present data and open circles are from Ref. [22].

TABLE IV: Parameters of the optical potentials for $p+{}^6\text{Li}$ at 72 MeV/nucleon [24] and $p+{}^6\text{He}$ at 71 MeV/nucleon ([27] and present work).

| | V_0 (MeV) | r_{0r} (fm) | a_r (fm) | W_0 (MeV) | r_{0i} (fm) | a_i (fm) | W_d (MeV) | r_{0id} (fm) | a_{id} (fm) | V_s (MeV) | r_{0s} (fm) | a_s (fm) |
|-----------------------------------|----------------|------------------|---------------|----------------|------------------|---------------|----------------|-------------------|------------------|----------------|------------------|---------------|
| Set-A $p+{}^6\text{Li}$ [24] | 31.67 | 1.10 | 0.75 | 14.14 | 1.15 | 0.56 | — | — | — | 3.36 | 0.90 | 0.94 |
| Set-B $p+{}^6\text{He}$ (Present) | 27.86 | 1.074 | 0.681 | 16.58 | 0.86 | 0.735 | — | — | — | 2.02 | 1.29 | 0.76 |
| Set-C $p+{}^6\text{He}$ [27] | 30.00 | 0.990 | 0.612 | 14.0 | 1.10 | 0.690 | 1.00 | 1.76 | 0.772 | 5.90 | 0.677 | 0.630 |

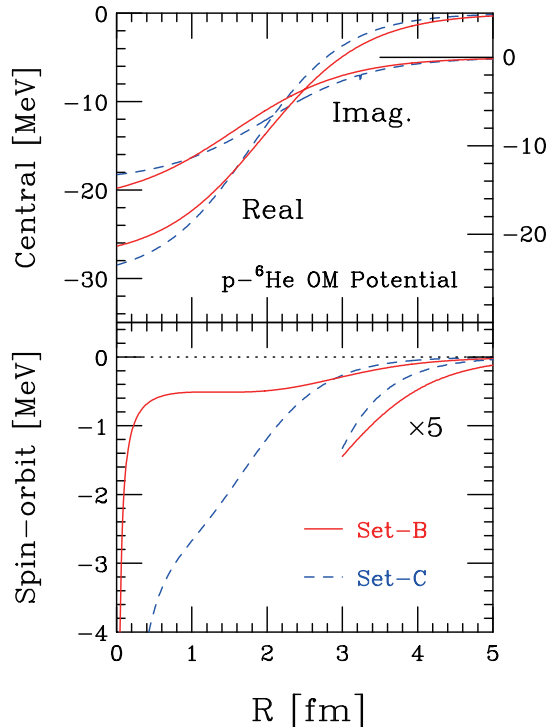


FIG. 10: (Color online) Radial dependences of the phenomenological optical potential (Set-B and Set-C in Table IV). Solid and dashed curves in the upper panel represent the real and imaginary parts of the central term. The lower panel shows the spin-orbit potential.

C potentials originates from that of the central terms as shown in the upper panel of Fig. 10. The reliability of the potential obtained in the present work is supported by the fact that two independent analyses yielded the similar results for the central terms. In contrast to the central terms, the spin-orbit terms of these two potentials are quite different, resulting in a large difference in A_y as shown in Fig. 9. Note that the present data are sensitive to the optical potential in a region of $R \gtrsim 1.5$ fm. The spin-orbit potential of Set-B is much shallower than that of Set-C at $R \lesssim 2.8$ fm, while it is deeper at larger radii. This is due to the small value of V_s and large values of r_{0s} and a_s of Set-B compared with those of Set-C. The phenomenological optical model analysis suggests that the A_y data can be reproduced only with a shallow and long-ranged spin-orbit potential.

The parameters of our spin-orbit potential are compared with those of neighboring even-even stable nuclei and with global potentials in Table V. Phenomenological optical potentials for the $p+{}^{16}\text{O}$ at 65 MeV and $p+{}^{12}\text{C}$ at 16–40 MeV are taken from Ref. [25] and Refs. [28, 29], respectively. In addition to these local potentials, we also examined the parameters of global optical potentials: CH89 [4] and Koning-Delaroche (KD) [5], of which applicable ranges are $E = 10\text{--}65$ MeV, $A = 40\text{--}209$ and $E = 0.001\text{--}200$ MeV, $A = 24\text{--}209$, respectively. While they are constructed for nuclei heavier than ${}^6\text{He}$, it is worthwhile comparing them, since the mass-number dependence of the parameters is relatively small. For example, the mass-number dependence appears only in r_{0s} in the case of CH89 [4] as:

$$\begin{aligned} V_s &= 5.9(1) \text{ MeV}, \\ r_{0s} &= 1.34(3) - 1.2(1)A^{-1/3} \text{ fm}, \\ a_s &= 0.63(2) \text{ fm}. \end{aligned}$$

Table V includes the parameters of these potentials for the nuclei within the applicable range. Incident energies of $E = 65$ MeV and $E = 71$ MeV were assumed here for CH89 and KD, respectively.

Firstly, we focus on r_{0s} and a_s to discuss the radial shape of the spin-orbit potential. Combination of different values of r_{0s} and a_s can provide similar results of A_y since the observable is sensitive to the surface region of the spin-orbit potential. We thus compare these parameters on the two-dimensional plane of r_{0s} and a_s as shown in Fig. 11. Parameters for the stable nuclei are mostly distributed in a region of $r_{0s} = 0.8\text{--}1.1$ fm and $a_s = 0.5\text{--}0.6$ fm, whereas that for ${}^6\text{He}$ is located in the upper right side of the figure. These large r_{0s} and/or a_s values indicate that the spin-orbit potential between a proton and a ${}^6\text{He}$ has a long-ranged nature compared with those for stable nuclei. The depth parameter V_s was also compared with the global systematics. The V_s value of $p+{}^6\text{He}$ potential was found to be 2.02 MeV for the best-fit potential (Set-B) and ranges between 1.15 and 2.82 MeV in the simultaneous confidence region for r_{0s} and a_s . On the other hand, those of stable nuclei are mostly distributed around 5 MeV as shown in Table V. Comparing these values, the depth parameter of the spin-orbit potential between a proton and a ${}^6\text{He}$ is found to be much smaller than those of stable nuclei.

The phenomenological analysis indicates that the spin-orbit potential between a proton and ${}^6\text{He}$ is characterized

| | V_s (MeV) | r_{0s} (fm) | a_s (fm) |
|--|-----------------------|-----------------------|-----------------|
| $p+{}^6\text{He}$, $E = 71$ MeV (Set-B) | 2.02 | 1.29 | 0.76 |
| $p+{}^{12}\text{C}$, $E = 40$ MeV [28] | 6.18 | 1.109 | 0.517 |
| $p+{}^{12}\text{C}$, $E = 16\text{--}40$ MeV [29] | 6.4 | 1.00 | 0.575 |
| $p+{}^{16}\text{O}$, $E = 65$ MeV [25] | 5.793 | 1.057 | 0.5807 |
| CH89, $E = 65$ MeV, $A = 40\text{--}209$ [4] | 5.9 ± 0.1 | $0.99\text{--}1.14$ | 0.63 ± 0.02 |
| KD, $E = 71$ MeV, $A = 24\text{--}209$ [5] | $4.369\text{--}4.822$ | $0.961\text{--}1.076$ | 0.59 |

TABLE V: Parameters of the spin-orbit term of phenomenological and global optical potentials.

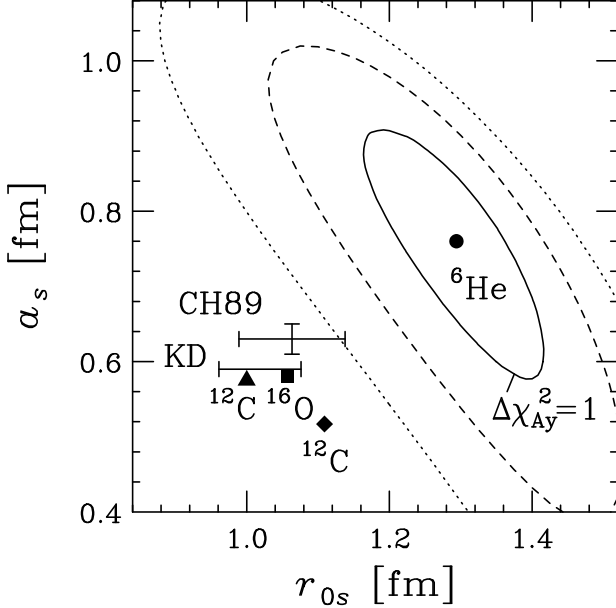


FIG. 11: Two-dimensional distribution of r_{0s} and a_s of phenomenological OM potentials for $p+{}^6\text{He}$ (closed circle), $p+{}^{12}\text{C}$ (closed triangle: Ref. [29], closed diamond: [28]), and $p+{}^{16}\text{O}$ (closed square: [25]). The solid contour indicates the simultaneous confidence region for the r_{0s} and a_s values for the $p+{}^6\text{He}$ as displayed in Fig. 8. Parameters of global OM potentials [4, 5] are also shown by solid lines which represent the A -dependence of r_{0s} .

by large r_{0s}/a_s and small V_s values yielding shallow and long-ranged radial dependence. Intuitively, these characteristics can be understood from the diffused density distribution of ${}^6\text{He}$. However, its microscopic origin can not be clarified by the phenomenological approach. To examine the microscopic origin of the characteristics of the $p+{}^6\text{He}$ interaction, microscopic and semi-microscopic analyses are required. Section V describes one of such analyses based on a cluster folding model for ${}^6\text{He}$.

V. SEMI-MICROSCOPIC ANALYSES

In this section, we examine two kinds of the folding potential, the cluster folding (CF) and the nucleon folding

(NF) ones. They are compared with the phenomenological optical model (OM) potential determined in the preceding section. The results of calculations of observables made by these potentials are compared with the experimental data.

In the CF potential, we adopt the αnn cluster model for ${}^6\text{He}$ and fold interactions between the proton and the valence neutrons, V_{pn} , with the neutron density in ${}^6\text{He}$ and those between the proton and the α core, $V_{p\alpha}$, with the α density in ${}^6\text{He}$. In the NF potential, we decompose the α core into two neutrons and two protons and fold the interactions between the incident proton and the four neutrons, V_{pn} , with the neutron density in ${}^6\text{He}$ and those between the incident proton and two target protons, V_{pp} , with the proton density in ${}^6\text{He}$.

The detailed expressions of such folding potentials are given in the following subsection, where the Coulomb interaction is considered in the p - p and p - α interactions respectively when compared with the corresponding scattering data but finally it is assumed to act between the proton and the ${}^6\text{He}$ target with $r_{0C} = 1.400$ fm [27].

A. Folding potentials

Denoting two valence neutrons by n_1 and n_2 , the CF potential U_{CF} is given as

$$U_{CF} = \int V_{pn_1} \rho_n^{\text{CF}}(r_1) d\mathbf{r}_1 + \int V_{pn_2} \rho_n^{\text{CF}}(r_2) d\mathbf{r}_2 + \int V_{p\alpha} \rho_\alpha^{\text{CF}}(r_\alpha) d\mathbf{r}_\alpha, \quad (3)$$

where \mathbf{r}_1 , \mathbf{r}_2 , and \mathbf{r}_α are the position vectors of n_1 , n_2 , and the α core from the center of mass of ${}^6\text{He}$, respectively. The neutron and α densities, ρ_n^{CF} and ρ_α^{CF} , are calculated by the αnn cluster model for ${}^6\text{He}$ [30, 31], where the condition $\mathbf{r}_1 + \mathbf{r}_2 + 4\mathbf{r}_\alpha = 0$ is considered as usual.

In the present work, we specify the potentials in the right hand side of Eq. (3) by the central plus spin-orbit (LS) type:

$$V_{pn_i} = V_{pn}^0(|\mathbf{r}_{pn_i}|) + V_{pn}^{\text{LS}}(|\mathbf{r}_{pn_i}|)\ell_{pn_i} \cdot (\boldsymbol{\sigma}_p + \boldsymbol{\sigma}_{n_i}),$$

where $i = 1, 2$ and

$$V_{p\alpha} = V_{p\alpha}^0(|\mathbf{r}_{p\alpha}|) + V_{p\alpha}^{\text{LS}}(|\mathbf{r}_{p\alpha}|)\ell_{p\alpha} \cdot \boldsymbol{\sigma}_p. \quad (4)$$

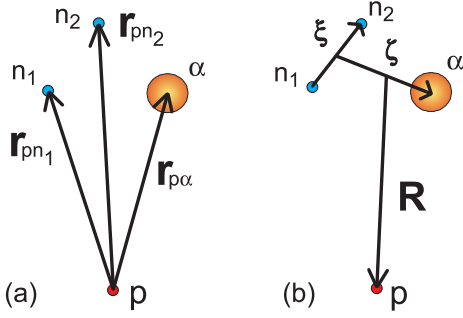


FIG. 12: (Color online) Coordinate systems for the cluster folding model.

Here, \mathbf{r}_{pn_1} , \mathbf{r}_{pn_2} , and $\mathbf{r}_{p\alpha}$ are defined in Fig. 12 (a), and $\mathbf{l}_{pn_1} = \mathbf{r}_{pn_1} \times (-i\hbar\nabla_{pn_1})$, etc.

In the following, we transform the set of coordinates $(\mathbf{r}_{pn_1}, \mathbf{r}_{pn_2}, \mathbf{r}_{p\alpha})$ to that of $(\boldsymbol{\xi}, \boldsymbol{\zeta}, \mathbf{R})$, which are defined in Fig. 12 (b), to describe the angular momenta \mathbf{l}_{pn_i} and $\mathbf{l}_{p\alpha}$ in terms of \mathbf{L} . The transformation is

$$\begin{aligned} \mathbf{r}_{pn_1} &= -\mathbf{R} - \frac{2}{3}\boldsymbol{\zeta} - \frac{1}{2}\boldsymbol{\xi}, & \mathbf{r}_{pn_2} &= -\mathbf{R} - \frac{2}{3}\boldsymbol{\zeta} + \frac{1}{2}\boldsymbol{\xi}, \\ \mathbf{r}_{p\alpha} &= -\mathbf{R} + \frac{1}{3}\boldsymbol{\zeta}, \end{aligned} \quad (5)$$

and consequently

$$\begin{aligned} \nabla_{pn_1} &= -\frac{1}{6}\nabla_{\mathbf{R}} - \frac{1}{2}\nabla_{\boldsymbol{\zeta}} - \nabla_{\boldsymbol{\xi}}, \\ \nabla_{pn_2} &= -\frac{1}{6}\nabla_{\mathbf{R}} - \frac{1}{2}\nabla_{\boldsymbol{\zeta}} + \nabla_{\boldsymbol{\xi}}, \\ \nabla_{p\alpha} &= -\frac{2}{3}\nabla_{\mathbf{R}} + \nabla_{\boldsymbol{\zeta}}. \end{aligned} \quad (6)$$

These relations lead to, for example,

$$\mathbf{l}_{pn_1} = (-\mathbf{R} - \frac{2}{3}\boldsymbol{\zeta} - \frac{1}{2}\boldsymbol{\xi}) \times [-i\hbar(-\frac{1}{6}\nabla_{\mathbf{R}} - \frac{1}{2}\nabla_{\boldsymbol{\zeta}} - \nabla_{\boldsymbol{\xi}})]. \quad (7)$$

Here, $\nabla_{\boldsymbol{\xi}}$ and $\nabla_{\boldsymbol{\zeta}}$ can be neglected, because these are the momenta for the internal degrees of freedom of ${}^6\text{He}$ and their expectation values are zero for a spherically symmetric nucleus [32]. Using $\frac{2}{3}\boldsymbol{\xi} + \frac{1}{2}\boldsymbol{\zeta} = -\mathbf{r}_1$, we get

$$\mathbf{l}_{pn_1} = \frac{1}{6}[\mathbf{L} - \mathbf{r}_1 \times (-i\hbar\nabla_{\mathbf{R}})], \quad (8)$$

which is independent of the special choice of the ${}^6\text{He}$ internal coordinates, $\boldsymbol{\xi}$ and $\boldsymbol{\zeta}$. To \mathbf{L} , \mathbf{r}_1 can contribute by its component along the \mathbf{R} direction [32], then

$$\mathbf{l}_{pn_1} = \frac{1}{6}\mathbf{L}(1 - \frac{\mathbf{r}_1 \cdot \mathbf{R}}{R^2}). \quad (9)$$

Similar expressions are obtained for \mathbf{l}_{pn_2} and $\mathbf{l}_{p\alpha}$. Setting $\frac{1}{2}(\boldsymbol{\sigma}_{n_1} + \boldsymbol{\sigma}_{n_2}) = 0$ and considering other quantities to appear in symmetric manners on 1 and 2, we obtain the p - ${}^6\text{He}$ potential as

$$U_{\text{CF}} = U_0^{\text{CF}}(R) + U_{\text{LS}}^{\text{CF}}(R)\mathbf{L} \cdot \boldsymbol{\sigma}_p, \quad (10)$$

with

$$\begin{aligned} U_0^{\text{CF}}(R) &= 2 \int V_{pn}^0(|\mathbf{r}_1 - \mathbf{R}|) \rho_n^{\text{CF}}(r_1) d\mathbf{r}_1 \\ &+ \int V_{p\alpha}^0(|\mathbf{r}_\alpha - \mathbf{R}|) \rho_\alpha^{\text{CF}}(r_\alpha) d\mathbf{r}_\alpha \end{aligned} \quad (11)$$

and

$$\begin{aligned} U_{\text{LS}}^{\text{CF}}(R) &= \frac{1}{3} \int V_{pn}^{\text{LS}}(|\mathbf{r}_1 - \mathbf{R}|) \left\{ 1 - \frac{\mathbf{r}_1 \cdot \mathbf{R}}{R^2} \right\} \rho_n^{\text{CF}}(r_1) d\mathbf{r}_1 \\ &+ \frac{2}{3} \int V_{p\alpha}^{\text{LS}}(|\mathbf{r}_\alpha - \mathbf{R}|) \left\{ 1 - \frac{\mathbf{r}_\alpha \cdot \mathbf{R}}{R^2} \right\} \rho_\alpha^{\text{CF}}(r_\alpha) d\mathbf{r}_\alpha \end{aligned}$$

In a way similar to the above development, we get the NF model potential U_{NF} . In this case, the relative coordinates between the incident proton and six nucleons in the ${}^6\text{He}$ nucleus are transformed to the proton- ${}^6\text{He}$ relative coordinate \mathbf{R} and a set of five independent internal coordinates of ${}^6\text{He}$. The obtained U_{NF} , which is independent on the choice of the set of the internal coordinates, is written as

$$U_{\text{NF}} = U_0^{\text{NF}}(R) + U_{\text{LS}}^{\text{NF}}(R)\mathbf{L} \cdot \boldsymbol{\sigma}_p, \quad (13)$$

with

$$\begin{aligned} U_0^{\text{NF}}(R) &= 2 \int V_{pp}^0(|\mathbf{r}_1 - \mathbf{R}|) \rho_p^{\text{NF}}(r_1) d\mathbf{r}_1 \\ &+ 4 \int V_{pn}^0(|\mathbf{r}_2 - \mathbf{R}|) \rho_n^{\text{NF}}(r_2) d\mathbf{r}_2 \end{aligned} \quad (14)$$

and

$$\begin{aligned} U_{\text{LS}}^{\text{NF}}(R) &= \frac{1}{3} \int V_{pp}^{\text{LS}}(|\mathbf{r}_1 - \mathbf{R}|) \left\{ 1 - \frac{\mathbf{r}_1 \cdot \mathbf{R}}{R^2} \right\} \rho_p^{\text{NF}}(r_1) d\mathbf{r}_1 \\ &+ \frac{2}{3} \int V_{pn}^{\text{LS}}(|\mathbf{r}_2 - \mathbf{R}|) \left\{ 1 - \frac{\mathbf{r}_2 \cdot \mathbf{R}}{R^2} \right\} \rho_n^{\text{NF}}(r_2) d\mathbf{r}_2 \end{aligned}$$

where ρ_n^{NF} and ρ_p^{NF} denote point neutron and proton densities, respectively.

B. Numerical evaluation of p - ${}^6\text{He}$ potentials

To evaluate the p - ${}^6\text{He}$ folding potentials as specified in the preceding section, we have to fix the following elements; the p - α interaction $V_{p\alpha}$, the p - p and p - n interactions V_{pp} and V_{pn} , and the densities in ${}^6\text{He}$, ρ_α , ρ_p and ρ_n . These are discussed in the following subsections, respectively.

1. p - α interactions

For $V_{p\alpha}$ used in the CF potential, we assume the standard WS potential such as given in Eq. (1). The parameters involved are searched so as to fit the data of $d\sigma/d\Omega$ and A_y in the p - α scattering at 72 MeV/nucleon

[23]. Particular attention was given to reproducing the observables in the forward angular region, since overall agreements with the data are not found in spite of the careful search of the parameters. Two typical parameter sets, with and without the volume absorption term, are labeled as Set-1 and Set-2 in Table VI. The results of calculations made with these potentials are compared with the data in Fig. 13, where the solid and dashed lines show those by Set-1 and Set-2 potentials, respectively. Both calculations describe the data up to $\theta \approx 100^\circ$ but do not reproduce those at backward angles, $\theta \gtrsim 120^\circ$. Such discrepancies between the calculated results and the measured data at the backward angles suggest participation of contributions of other reaction mechanisms, such as knock-on type exchange scattering of the proton with target nucleons. Such possible extra mechanisms will be disregarded at present since we are concerned with the p - α one-body potential. In our CF calculations, we adopt the potentials with the above parameter sets as $V_{p\alpha}$. However, the validity of the CF potential thus obtained is limited to forward scattering angles, a low momentum transfer region, of $p+{}^6\text{He}$ scattering. The real and imaginary parts of $V_{p\alpha}^0$ and the real part of $V_{p\alpha}^{\text{LS}}$ for the above parameter sets are displayed in the upper and lower panels of Fig. 14. Although Set-1 (dashed) and Set-2 (solid) potentials have rather different $r_{p\alpha}$ dependence, as shown later, this difference is moderated in the folding procedure so yielding similar CF potentials.

2. p - p and p - n interactions

For V_{pn} and V_{pp} used in the CF and NF potentials, we adopt the complex effective interaction, CEG [33–35], where the nuclear force [36] is modified by the medium effect which takes account of the virtual excitation of nucleons of the nuclear matter up to $10k_F$ by the g -matrix theory. The nuclear force is composed of Gaussian form factors and the parameters contained are adjusted to simulate the matrix elements of the Hamada-Johnston potential [37]. The CEG interaction has been successful in reproducing $d\sigma/d\Omega$ and A_y measured for the proton elastic scattering by many nuclei in a wide incident energy range, $E_p = 20$ – 200 MeV, in the framework of the folding model [33–35]. It has been shown that the imaginary part of the folding potential given by the CEG interaction is slightly too large to reproduce experimental N-A scattering [33, 35]. In the present calculation, therefore, we adopt the normalizing factor $N_I = 0.7$ for the imaginary part of the CEG interaction. However, calculations with $N_I = 1.0$ do not give an essential change to the results.

3. Densities of α , p and n in ${}^6\text{He}$

The densities ρ_n^{CF} and ρ_α^{CF} for the CF calculation are obtained by applying the Gaussian expansion

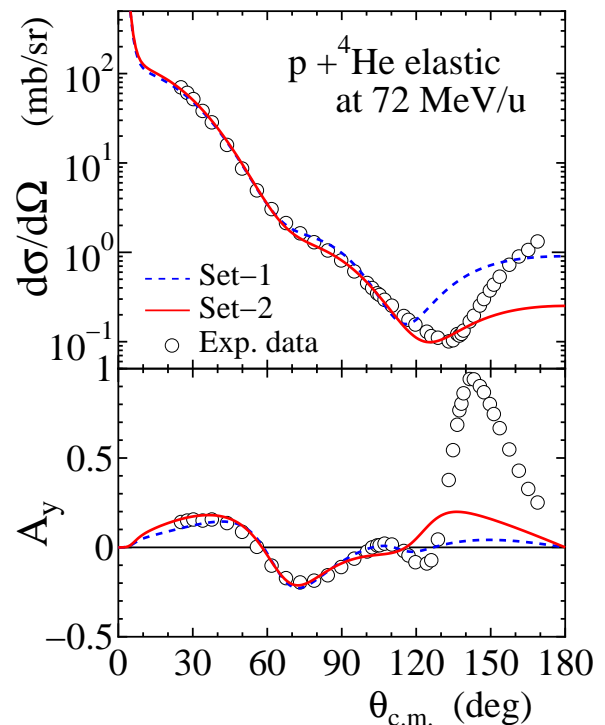


FIG. 13: (Color online) Angular distribution of the cross section and A_y for the $p+{}^4\text{He}$ elastic scattering at 72 MeV/nucleon. The solid and dashed lines are the optical model calculations with Set-1 and Set-2 parameters, respectively. The experimental data are taken from Ref. [23].

method [30, 31] to the αnn cluster model of ${}^6\text{He}$. This method has been successful in describing structures of various few-body systems as well as ${}^6\text{He}$ [30, 31]. As for the n - n interaction, we choose AV8' interaction [38]. It is reasonable to use a bare (free space) n - n interaction between the two valence neutrons in ${}^6\text{He}$ as they are dominantly in a region of low density. As for the α - n interaction, we employ the effective α - n potential in Ref. [39], which was designed to reproduce well the low-lying states and low-energy-scattering phase shifts of the α - n system. The depth of the α - n potential is modified slightly to adjust the ground-state binding energy of ${}^6\text{He}$ to the empirical value. In Fig. 15(a), the densities obtained are shown as functions of r , the distance from the center of mass of ${}^6\text{He}$, where ρ_α^{CF} is localized in a relatively narrow region around the center, while ρ_n^{CF} is spread widely.

The NF calculation depends on the assumptions made for the densities of the two protons and four neutrons in ${}^6\text{He}$ as well as those made for the p - p and p - n interactions [18]. At present, to see the essential role of clustering the four nucleons into the α -particle core, we use the densities of the proton and the neutron in the α obtained by decomposing the density of the point α , ρ_α^{CF} , to the densities of the constituent nucleons with a one-range Gaussian form factor with range 1.40 fm. The

TABLE VI: Parameters for the optical potentials for $p+{}^4\text{He}$ at 72 MeV/nucleon.

| | V_0 (MeV) | r_{0r} (fm) | a_r (fm) | W_0 (MeV) | r_{0i} (fm) | a_i (fm) | W_d (MeV) | r_{0id} (fm) | a_{id} (fm) | r_{0C} (fm) | V_s (MeV) | r_{0s} (fm) | a_s (fm) |
|-------|----------------|------------------|---------------|----------------|------------------|---------------|----------------|-------------------|------------------|------------------|----------------|------------------|---------------|
| Set-1 | 64.13 | 0.7440 | 0.2562 | 6.338 | 1.450 | 0.2089 | 46.23 | 1.320 | 0.1100 | 1.400 | 2.752 | 1.100 | 0.2252 |
| Set-2 | 54.87 | 0.8566 | 0.09600 | — | — | — | 31.97 | 1.125 | 0.2811 | 1.400 | 3.925 | 0.8563 | 0.4914 |

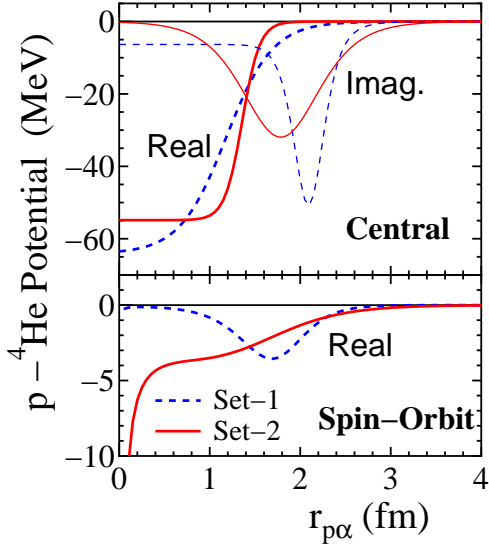


FIG. 14: (Color online) Optical potentials for the $p+{}^4\text{He}$ elastic scattering at 72 MeV/nucleon. The thick dashed (solid) lines are for the real part of Set-1 (Set-2) potential and the thin dashed (solid) lines are for the imaginary part.

total nucleon densities of ${}^6\text{He}$, ρ_p^{NF} , and ρ_n^{NF} , where the latter includes the contribution of the valence neutrons, are displayed in Fig. 15(b). The neutron density ρ_n^{NF} has a longer tail than the proton one ρ_p^{NF} due to the presence of the valence neutrons. In Refs. [40, 41] the nucleon densities of ${}^6\text{He}$ were calculated in a more sophisticated way. They produced densities similar to the present ones for the protons and neutrons. These two kinds of nucleon densities provide similar results in the NF calculation of $d\sigma/d\Omega$ and A_y of the $p+{}^6\text{He}$ scattering. Thus, in the following, we will discuss U_{NF} as formed using the densities shown in Fig. 15(b).

4. $p-{}^6\text{He}$ folding potentials

In Fig. 16, the resultant $p-{}^6\text{He}$ potentials, U_{CF} and U_{NF} , are compared with each other as well as with the optical model potential U_{OM} . The CF potentials calculated by the two sets of $V_{p\alpha}$ in Table VI, say $U_{\text{CF-1}}$ and $U_{\text{CF-2}}$, are shown by long-dashed and solid lines in Fig. 16(a), respectively. The folding procedure gives similar results in both cases. The contribution of V_{pn} is displayed by short-dashed lines in the figure, which is found to be mostly small. Especially, in the spin-orbit poten-

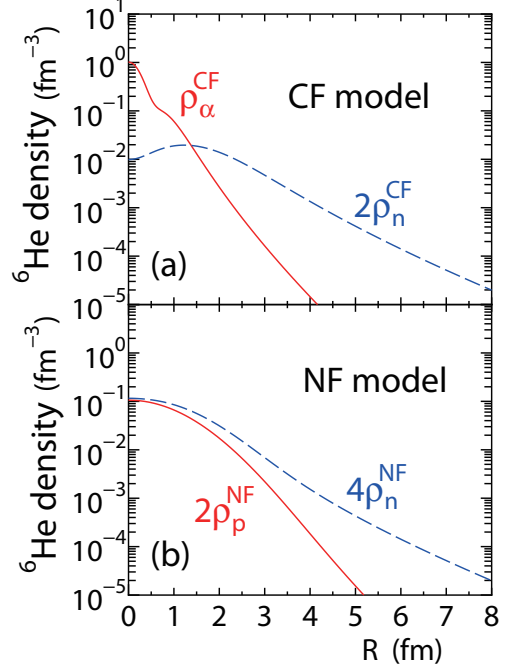


FIG. 15: (Color online) The densities of α , p , and n in ${}^6\text{He}$ used in folding models. The ρ_α^{CF} and ρ_n^{CF} in panel (a) are used in the CF calculation. The ρ_p^{NF} and ρ_n^{NF} in panel (b) are used in the NF calculation. All densities are normalized as $4\pi \int \rho_x r^2 dr = 1$, where $x = \alpha, n$, and p .

tial, the contribution from V_{pn} is one order of magnitude smaller than that from $V_{p\alpha}$. The main contribution to U_{CF} arises from the interaction $V_{p\alpha}$ except for the central real potential at $R \gtrsim 3$ fm, which is dominated by the V_{pn} contribution. This is supposed to be the reflection of the extended neutron density shown in Fig. 15 and produce significant contributions to the observables as discussed later.

In Fig. 16(b), U_{CF} due to Set-2 of $V_{p\alpha}$, U_{NF} , and U_{OM} are shown by solid, dot-dashed, and short-dashed lines, respectively. First we consider the central part of the potentials. For small R , the real part of U_0^{CF} is deeper than those of U_0^{NF} and U_0^{OM} , while for large R , U_0^{CF} is shallower than other two. In the imaginary part, the magnitude of U_0^{CF} is much bigger than those of the other two potentials. This will compensate the deficiency of the real part of U_0^{CF} at large R , for example in the calculation of the cross section. On the other hand, the spin-orbit part of U_{OM} has larger magnitude for $R \gtrsim 2$ fm and thus has a longer range compared with those of other

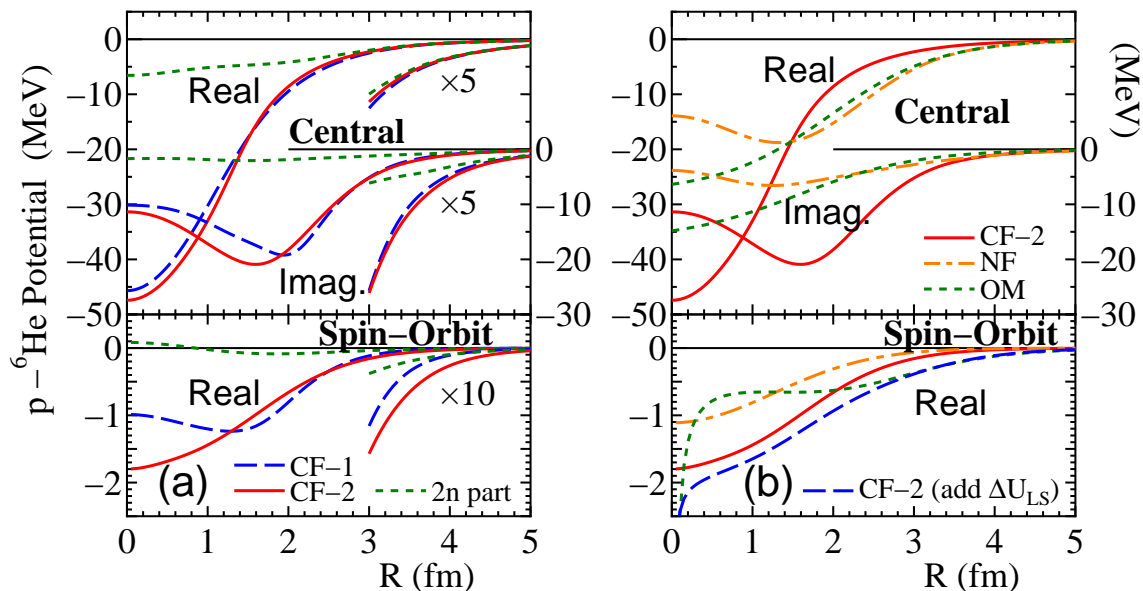


FIG. 16: (Color online) Potentials between proton and ${}^6\text{He}$. (a): The long-dashed (solid) lines are the CF calculation with Set-1 (Set-2) parameters for $V_{p\alpha}$. The short-dashed lines show the contribution of the valence two neutrons to the CF potential. (b): The solid lines are the CF calculation with Set-2 parameters, the dot-dashed lines are the NF one and the short-dashed lines are the phenomenological optical potential. The CF spin-orbit potential corrected by ΔU_{LS} term is shown by the long-dashed line (see text for detail).

two potentials. Such long-range nature of the spin-orbit interaction is a characteristic feature of the spin-orbit part of U_{OM} as described in Section IV. This is discussed later in more detail with relation to A_y .

C. Comparison between experiments and calculations in $p+{}^6\text{He}$ scattering

In the following, the $d\sigma/d\Omega$ and A_y for $p-{}^6\text{He}$ elastic scattering calculated using U_{CF} , U_{NF} , and U_{OM} are compared with the data taken at 71 MeV/nucleon. In Fig. 17(a) the results obtained using the two CF potentials, U_{CF-1} and U_{CF-2} , are shown by long-dashed and solid lines, respectively. Both results are very similar to each other and well describe the data of $d\sigma/d\Omega$, except for large angles where the calculations overestimates the data by small amounts. The calculations also describe the angular dependence of the measured A_y up to $\theta \simeq 55^\circ$. These successes basically support the CF potential as a reasonable description of the scattering. The discrepancies at large angles, i.e. a large momentum transfer region, may be related to the limitation of the validity of $V_{p\alpha}$ used in the folding, as discussed in the subsection VB.

In Fig. 17(a), the results of the calculation made using the NF potential are shown by dot-dashed lines. They do not reproduce the data well. The calculation gives a deep valley around $\theta \simeq 53^\circ$ in the angular distribution of $d\sigma/d\Omega$ and a large positive peak at the corresponding angle of the A_y angular distribution. These features

do not exist in the data. Since the present nucleon densities originated from the CF model ones, the essential difference between the CF and NF potentials will be produced by the use of the different interactions. Thus, the CF calculation will owe its successes to the inclusion of the characteristics of the realistic $p-\alpha$ interaction into the $p-{}^6\text{He}$ potential.

It is interesting to examine if the α core in ${}^6\text{He}$ is somewhat diffused compared with a free α -particle, due to the interactions from the valence neutrons. For that purpose, we increased the radius and diffuseness parameters, r_0 and a , in $V_{p\alpha}$ potential as r_0 to $1.1 r_0$ and a to $a + 0.1$ fm. The depth parameters were changed to keep constant the values of the corresponding volume integrals. The effect of this change is shown by the short-dashed lines in Fig. 17(a), where reproduction of the data is improved somewhat, especially in $d\sigma/d\Omega$ at large angles.

In Fig. 17(b), the contributions of the valence neutrons are demonstrated for the CF-2 calculation. As is speculated from the analyses of the form factors of the potential in Fig. 16(a), the dominant contribution to the observables in the CF calculation arises from $V_{p\alpha}$ displayed by the dot-dashed lines in Fig. 17(b). However, the valence neutrons produce indispensable corrections to the observables. That is, the pn central interaction decreases $d\sigma/d\Omega$ at large angles, giving remarkable improvements of the agreement with the data as shown by the dashed lines. The pn interaction also contributes to A_y by a considerable amount through the central part. A detailed examination of the calculation revealed that such corrections were due to the V_{pn} part of the folding

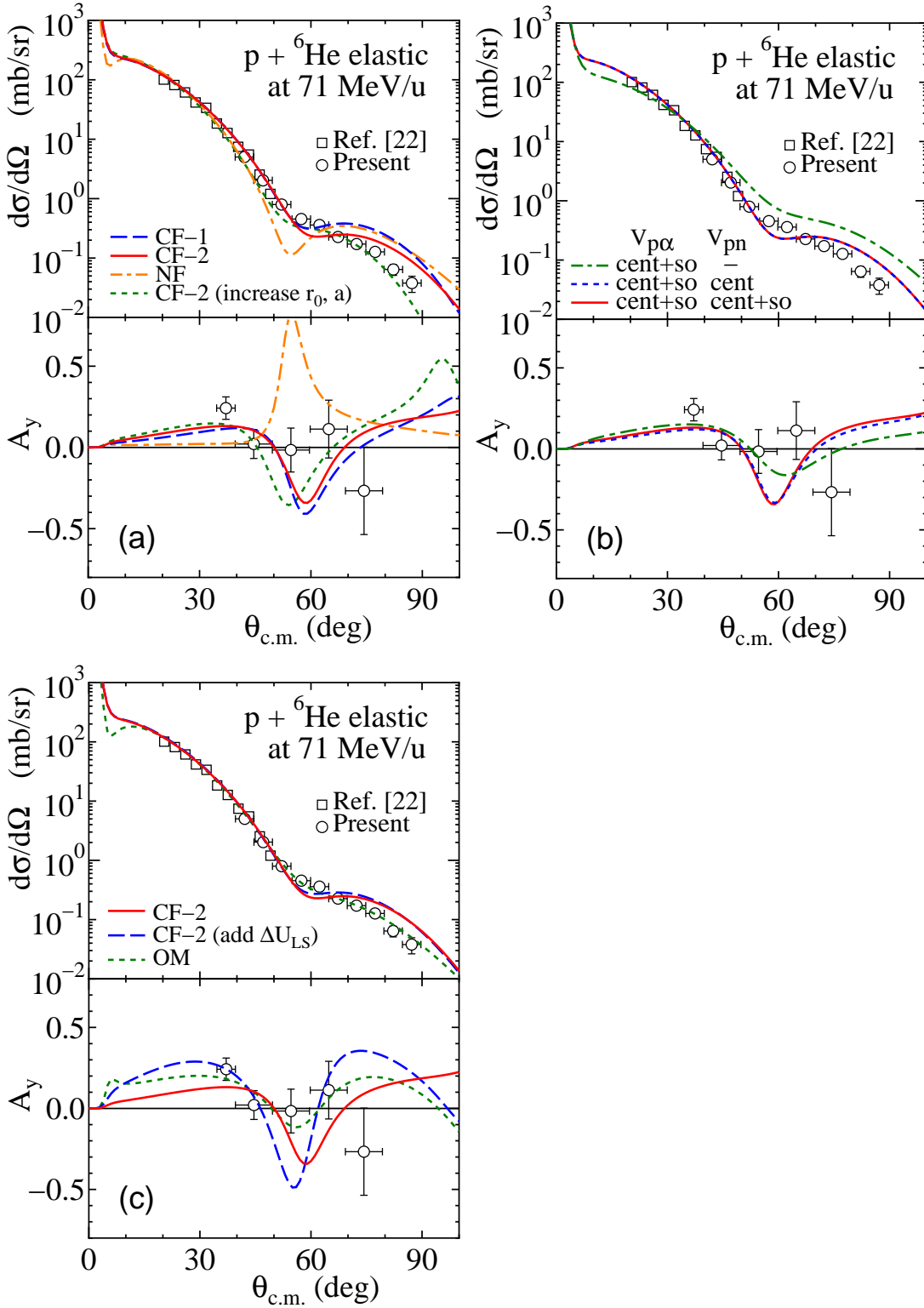


FIG. 17: (Color online) Angular distribution of the cross section and A_y for the $p + {}^6\text{He}$ elastic scattering at 71 MeV/nucleon. The experimental data are denoted by circles (present) and squares (Ref. [22]). (a): The long-dashed (solid) lines are the CF calculation in which Set-1 (Set-2) parameters are used for $V_{p\alpha}$. The dot-dashed lines are the NF calculation. (b): The dashed lines and the solid ones include the V_{pn} interaction, where the formers neglect the spin-orbit part of V_{pn} . The dash-dotted lines include only $V_{p\alpha}$ interaction. (c): The solid lines are the CF calculation with Set-2 parameters for $V_{p\alpha}$ and the short-dashed lines are the OM calculation. The long-dashed lines are the CF calculation with Set-2 parameters for $V_{p\alpha}$ where ΔU_{LS} is added (see text for detail).

central potential in a R region between $R = 2$ fm and 4 fm (see Fig. 16(a)). The spin-orbit part of V_{pn} gives almost no effect to the observables as shown by the solid lines in Fig. 17(b). This is consistent with the result shown by Crespo *et al.* [42] in a study at higher incident energy.

In Fig. 17(c), we compared the results of the CF-2 calculation (solid lines) with those of the OM calculation in the preceding section (long-dashed lines) as well as with the data. In the optical model analysis, the experimental data can be reproduced only with a shallow and long-ranged spin-orbit potential. Compared with this potential, the spin-orbit part of CF-2 potential has a shorter range as displayed by a solid line in the lower panel of Fig. 16(b). To investigate the role of the long tail in the spin-orbit potential, we calculated the observables by adding a weak but long-range spin-orbit interaction ΔU_{LS} to the CF interaction. This correction is assumed to be the Thomas type as

$$\Delta U_{LS}(R) = v_{\text{add}} \frac{2}{R} \frac{d}{dR} \left[1 + \exp \left\{ (R - 6^{1/3} r_{\text{add}}) / a_{\text{add}} \right\} \right]^{-1} \quad (16)$$

For simplicity, we adopt $v_{\text{add}} = 1$ MeV, $r_{\text{add}} = 1.5$ fm, and $a_{\text{add}} = 0.7$ fm where the large magnitudes of r_{add} and a_{add} are consistent with the characteristics of the magnitudes of r_{0s} and a_s of the OM potential discussed in Sec. IV. The calculated observables are displayed in Fig. 17(c) by short-dashed lines, where $d\sigma/d\Omega$ is little affected but A_y receives a drastic change, i.e. the angular distribution of A_y is now similar to that by the OM calculation in a global sense showing qualitative improvements in comparison with the data. To see the contribution of ΔU_{LS} to the potential, we plot $U_{LS}^{\text{CF}} + \Delta U_{LS}$ in Fig. 16(b) by long-dashed lines, where the new spin-orbit potential becomes very close to that of the OM potential at $R \gtrsim 2.5$ fm. It is indicated that the long tail of the spin-orbit potential is particularly important in reproducing the angular distribution of A_y , while its microscopic origin is still to be investigated. When some corrections which increase the range of the spin-orbit interaction are found, they will be effective for improving the CF calculation.

VI. MICROSCOPIC MODEL ANALYSES

In this section, we will describe the theoretical analysis of the present data by a microscopic model developed in Ref. [7]. In this model, one can predict the scattering observables such as cross sections and analyzing powers with one run of the relevant code (DWBA98) with no adjustable parameter. Complete details as well as many examples of use of this coordinate space microscopic model approach are to be found in the review [7]. Use of the complex, non-local, nucleon-nucleus optical potentials defined in that way, without localization of the exchange amplitudes, has given predictions of differential cross sections and spin observables that are in good agreement with data from many nuclei (^3He to ^{238}U)

and for a wide range of energies (40 to 300 MeV). Crucial to that success is the use of effective nucleon-nucleon (NN) interactions built upon NN g -matrices. The effective NN interactions are complex, energy and density dependent, admixtures of Yukawa functions. They have central, two-nucleon tensor and two-nucleon spin-orbit character. The NA optical potentials result from folding those effective interactions with the one-body density matrix elements (OBDME) of the ground state in the target nucleus. Antisymmetrization of the projectile with all target nucleons leads to exchange amplitudes, making the microscopic optical potential non-local. For brevity, the optical potentials that result are called g -folding potentials. Another application has been in the prediction of integral observables of elastic scattering of both protons and neutrons, with equal success [43]. Thus, the method is known now to give good predictions of both angular-dependent and integral observables.

It is important to note that the level of agreement with data in the g -folding approach depends on the quality of the structure model that is used. Due to the character of the hadron force, proton scattering is preferentially sensitive to the neutron matter distributions of nuclei; a sensitivity seen in a recent assessment, using proton elastic scattering, of diverse Skyrme-Hartree-Fock model structures for ^{208}Pb [44].

A. Structure of ^6He used

^6He is a two-neutron halo nucleus and has been described well by shell model calculations. In calculation of the g -folding potential for protons interacting with ^6He , a complete $(0+2+4)\hbar\omega$ shell model calculation has been made to specify the ground state OBDME. Essentially they are the occupation numbers which define the matter densities of the nucleus.

In the present study, we assume three sets of the single-nucleon (SN) wave functions for ^6He . One is the oscillator wave functions with an oscillator length of 2.0 fm (HO set). However, a neutron-halo character of ^6He can not be given by the oscillator wave function whatever oscillator length is used as shown by the dashed curve in the lower panel of Fig. 18. Thus, we assume two sets of SN wave functions defined in Woods-Saxon (WS) potentials. One of them is obtained by taking the geometry of the potential from that found appropriate in Ref. [7], where electron form factors and proton scattering from $^6,7\text{Li}$ are studied. That study provided a set of SN wave functions that we specify as WS nonhalo set since the p -shell nucleons were all reasonably bound. The extended neutron matter character of ^6He is found by choosing the binding energy of the halo-neutron orbits to give the single-neutron separation energy (1.8 MeV) to the lowest energy resonance in ^5He . The set of SN wave functions that result are specified as WS halo set. The associated density profile has the extensive neutron density coming from the halo. Density profiles given by the various sets

of SN wave functions are shown in Fig. 18. The dashed, solid, and dot-dashed curves show the density distributions of HO, WS halo, and WS nonhalo sets, respectively. The difference between proton distributions of WS halo and WS nonhalo sets can not be seen.

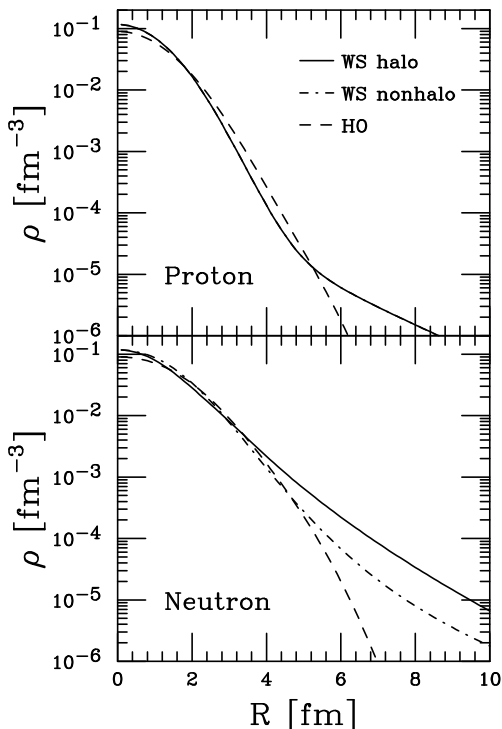


FIG. 18: The (model) proton and neutron densities are shown in the upper and lower panels, respectively. The solid, dot-dashed, and dashed curves represent those obtained with WS halo, WS nonhalo, and HO sets, respectively.

Use of WS halo set in analyses of 40.9 MeV/nucleon data [45] gave a value of 406 mb for the reaction cross section, which is in good agreement with the measured value. Additional evidence for WS halo set is given by the root mean square (r.m.s.) radius of the matter distribution, which is most sensitive to characteristics of the outer surface of a nucleus. Using WS nonhalo set of the SN wave functions gave an r.m.s. radius for ${}^6\text{He}$ of 2.30 fm, which is much smaller than the expected value of 2.54 fm. On the other hand, using WS halo set gave an r.m.s. radius for ${}^6\text{He}$ of 2.59 fm in good agreement with that expectation.

B. Differential cross sections and analyzing powers

The cross sections and analyzing powers for the $p+{}^6\text{He}$ elastic scattering at 71 MeV/nucleon are shown in the top and bottom panels of Fig. 19, respectively. The calculated results shown therein by the dashed lines were found using the g -folding potential obtained with HO set

of SN wave functions. This calculation does not give a satisfactory result; especially in the case of the analyzing power. The solid curves show results found using WS halo set while those depicted by the dot-dashed curves are those found with WS nonhalo set. Of these the halo description gives the better match to data especially at the larger scattering angles. This result is consistent with the findings from analyses of lower energy scattering data at 40.9 MeV/nucleon [45] and at 24.5 MeV/nucleon [46].

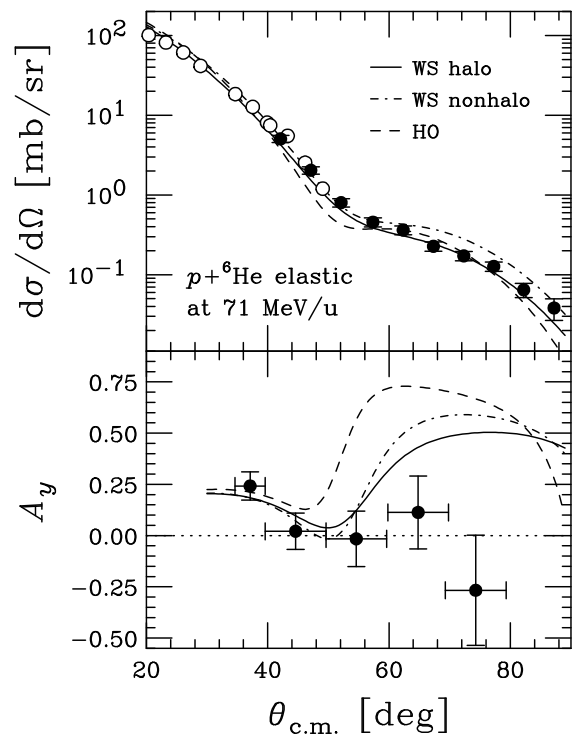


FIG. 19: Differential cross sections and analyzing powers of the $p+{}^6\text{He}$ elastic scattering at 71 MeV/nucleon (open circles: Ref. [22], closed circles: present work). Three curves are results of g -matrix folding calculation with ${}^6\text{He}$ densities presented in Fig. 18.

In fact, the differential cross sections calculated with WS halo set match the data so well that one does not need to contemplate any adjustment. However, the story is not so simple when one also considers the analyzing power data. At forward scattering angles, both WS sets reasonably match the data. But neither WS result produces the distinctive trend of small values found at larger scattering angles. Nonetheless the best result is that found on using WS halo set of SN functions. Given that the cross section values in the region of 60° to 90° is of an order of 0.1 mb/sr, the limitations in the present microscopic model formulation of the reaction dynamics may be the problem.

VII. SUMMARY

The vector analyzing power has been measured for the elastic scattering of ${}^6\text{He}$ from polarized protons at 71 MeV/nucleon to investigate the characteristics of the spin-orbit potential between the proton and the ${}^6\text{He}$ nucleus. Measurement of the polarization observable was realized in the RI-beam experiment by using the newly constructed solid polarized proton target, which can be operated in a low magnetic field of 0.1 T and at high temperature of 100 K. The measured $d\sigma/d\Omega$ of the $p+{}^6\text{He}$ elastic scattering were almost identical to those of the $p+{}^6\text{Li}$. On the other hand, the A_y were found to be largely different from those of the $p+{}^6\text{Li}$ and rather similar to those of the $p+{}^4\text{He}$ elastic scattering.

To extract the gross feature of the spin-orbit interaction between a proton and ${}^6\text{He}$, an optical model potential was determined phenomenologically by fitting the experimental data of $d\sigma/d\Omega$ and A_y . Compared with the global systematics of the potentials for stable nuclei, it is indicated that the spin-orbit potential for ${}^6\text{He}$ is characterized by a small value of V_s and large values of r_{0s} and a_s , namely by a shallow and long-ranged radial shape. Such characteristics might be the reflection of the diffused density of the neutron-rich ${}^6\text{He}$ nucleus.

The cluster folding calculation was carried out to get a deeper insight into the optical potential, assuming the $\alpha+n+n$ cluster structure for ${}^6\text{He}$. In addition, nucleon folding calculations were also performed by decomposing the α core into four nucleons. The experimental data could not be reproduced by the nucleon folding calculation, whereas the αnn cluster folding calculation gives the reasonable agreements with the data. Thus, this indicates that it is important to take into account of the α -clusterization in the description of $p+{}^6\text{He}$ elastic scattering. The cluster folding calculation shows that the dominant contribution to the $p+{}^6\text{He}$ potential arises from the interaction between the proton and the α core. Especially, in the spin-orbit potential, the contribution of the interaction between the proton and valence neutrons was found to be much smaller than the α core contribution. However, the measured cross section at large angles can not be understood without the contribution from the scattering by the valence neutrons. Comparison of the phenomenological optical potential and the cluster folding one indicates that the long-range nature of the spin-orbit potential is important in reproducing the A_y data at large angles. The microscopic origin of such a long tail is still to be investigated.

The data were also compared with the predictions obtained from a fully microscopic g -folding model. Three sets of single nucleon wave functions were tried since other details of the calculation were predetermined. The model, which has been successful in analyzing $p+{}^6\text{He}$ scattering cross sections in the past [44], again gives good reproduction of the data in the present case when the bound state wave functions specify that ${}^6\text{He}$ has a neutron halo. However, the match to the data, in particular

the analyzing power, is not perfect. This may indicate limitation of the structure model used and/or of unaccounted reaction mechanisms that influence the larger momentum transfer results.

This work has demonstrated the capability of the solid polarized proton target in low magnetic field and high temperature to probe the new aspects of the reaction involving unstable nuclei. Future polarization studies of such kinds will provide us with valuable information on the reaction and structure of unstable nuclei.

Acknowledgments

We thank the staffs of RIKEN Nishina Center and CNS for the operation of the accelerators and ion source during the measurement. S. S. acknowledges financial support by a Grant-in-Aid for JSPS Fellows (No. 18-11398). This work was supported by the Grant-in-Aid for Scientific Research No. 17684005 of the Ministry of Education, Culture, Sports, Science, and Technology of Japan.

Appendix A: Absolute measurement of target polarization

In the case of conventional solid polarized targets, the NMR signal usually is related to the absolute magnitude of the polarization by measuring the target polarization under the state of thermal equilibrium (TE). However, measurement of the TE polarization is quite difficult in our target. The first reason for this is that the TE polarization is very small in a low magnetic field and at high temperature, since it is represented by $P_{\text{TE}} = \tanh\left(\frac{\mu B}{2kT}\right)$, where μ , B , and T are the magnetic moment of proton, the field strength, and the temperature, respectively. The second reason is that the sensitivity of the present NMR system is not sufficiently high since the target design is optimized for scattering experiments.

One of the simple methods to measure the absolute target polarization would be the measurement of the spin-dependent asymmetry $\epsilon = P_y A_y$ for the proton elastic scattering whose analyzing power A_y are known. In the present study, we measured the spin-asymmetry for the $p+{}^4\text{He}$ elastic scattering at 80 MeV/nucleon. The A_y have already been measured by Togawa *et al* [47]. The use of the $p+{}^4\text{He}$ scattering is profitable since we can measure the ϵ with the same experimental setup as that for the $p+{}^6\text{He}$ measurement only by changing settings of the fragment separator RIPS to produce a secondary ${}^4\text{He}$ beam. The profile of the ${}^4\text{He}$ beam on the target was tuned to be almost same as that of the ${}^6\text{He}$ beam.

Figure 20 shows A_y of the $p+{}^4\text{He}$ elastic scattering at 80 MeV/nucleon. The open circles represent the previous data [47], while the closed ones show the present data whose magnitudes are scaled to the previous ones.

From the scaling factor, the average polarization during the $p+{}^4\text{He}$ measurement was determined to be $P_y = 12.3 \pm 2.4\%$. The relative uncertainty of the polarization $\Delta P_y/P_y$, which was 19% in the present work, resulted from the statistics of the $p+{}^4\text{He}$ scattering events. Future development of the NMR system would be required for determining the absolute polarization more precisely without losing beam time.

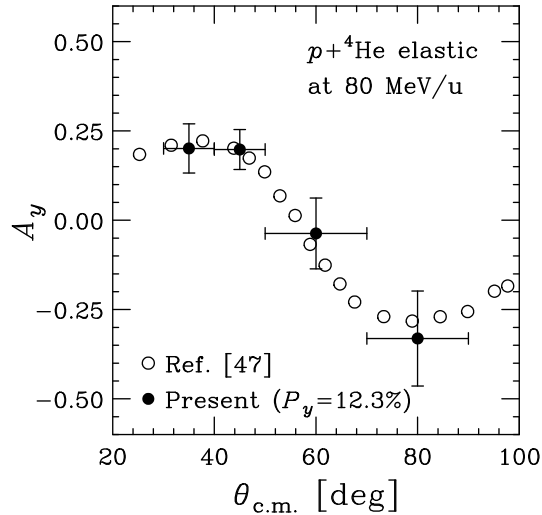


FIG. 20: Analyzing powers of the $p+{}^4\text{He}$ elastic scattering at 80 MeV/nucleon. Closed circles indicate the present data where $P_y = 12.3\%$ is assumed. Open circles represent the reference data taken from Ref. [47].

-
- [1] C. L. Oxley *et al.*, Physical Review **91**, 419 (1953).
[2] O. Chamberlain *et al.*, Physical Review **102**, 1659 (1956).
[3] E. Fermi, Nuovo Cimento **10**, 407 (1954).
[4] R. L. Varner *et al.*, Physics Reports (Review Section of Physics Letters) **201**, 58 (1991).
[5] A. Koning and J. Delaroche, Nuclear Physics A **713**, 231 (2003).
[6] F. Brieva and J. Rook, Nucl. Phys. A **297**, 1978 (206).
[7] K. Amos *et al.*, Advances in Nuclear Physics A **25**, 275 (2000).
[8] I. Tanihata *et al.*, Physics Letters B **160**, 380 (1985).
[9] D. Crabb and W. Meyer, Annu. Rev. Nucl. Part. Sci. **47**, 1997 (67).
[10] S. Goertz, W. Meyer, and G. Reicherz, Prog. Part. Nucl. Phys. **49**, 403 (2002).
[11] T. Wakui *et al.*, Nuclear Instruments and Methods in Physics Research A **526**, 182 (2004).
[12] T. Uesaka *et al.*, Nuclear Instruments and Methods in Physics Research A **526**, 186 (2004).
[13] T. Wakui *et al.*, Nuclear Instruments and Methods in Physics Research A **550**, 521 (2005).
[14] M. Hatano *et al.*, European Physical Journal A Supplement **25**, 255 (2005); M. Hatano, Ph.D. thesis, University of Tokyo, 2003.
[15] T. Wakui, Proc. XIth Int. Workshop on Polarized Ion Sources and Polarized Gas Targets 2005, edited by T. Uesaka, H. Sakai, A. Yoshimi, and K. Asahi (World Scientific, Singapore, 2007).
[16] D. Sloop, T. Yu, T. Lin, and S. Weissman, Journal of Chemical Physics **75**, 3746 (1981).
[17] A. Henstra, P. Dirksen, and W. T. Wenckebach, Physics Letters A **134**, 134 (1988).
[18] T. Uesaka *et al.*, Physical Review C **82**, 021602(R) (2010).
[19] A. Yoshida *et al.*, Nuclear Instruments and Methods in Physics Research A **590**, 204 (2008).
[20] T. Kubo *et al.*, Nuclear Instruments and Methods in Physics Research B **70**, 309 (1992).
[21] B. T. Ghim *et al.*, Journal of Magnetic Resonance A **120**, 72 (1996).
[22] A. Korshennikov *et al.*, Nuclear Physics A **617**, 45 (1997).
[23] S. Burzynski *et al.*, Physical Review C **39**, 56 (1989).
[24] R. Henneck *et al.*, Nuclear Physics A **571**, 541 (1994).
[25] H. Sakaguchi *et al.*, Physical Review C **26**, 944 (1982).
[26] J. Raynal, ECIS code, CEA-R2511 Report, unpublished,

- 1965.
- [27] D. Gupta, C. Samanta, and R. Kanungo, Nuclear Physics A **674**, 77 (2000).
- [28] M. Fricke, E. Gross, B. Morton, and A. Zucker, Physical Review **156**, 1207 (1967).
- [29] E. Fabrici *et al.*, Physical Review C **21**, 830 (1980).
- [30] E. Hiyama *et al.*, Physical Review C **53**, 2075 (1996).
- [31] E. Hiyama, Y. Kino, and M. Kamimura, Progress in Particle and Nuclear Physics **51**, 223 (2003).
- [32] L. Rikus and H. von Geramb, Nuclear Physics A **426**, 496 (1984).
- [33] N. Yamaguchi, S. Nagata, and T. Matsuda, Progress of Theoretical Physics **70**, 459 (1983).
- [34] S. Nagata, M. Kamimura, and N. Yamaguchi, Progress of Theoretical Physics **73**, 512 (1985).
- [35] N. Yamaguchi, S. Nagata, and J. Michiyama, Progress of Theoretical Physics **76**, 1289 (1986).
- [36] R. Tamagaki, Progress of Theoretical Physics **39**, 91 (1968).
- [37] T. Hamada and I. Johnston, Nuclear Physics **34**, 382 (1962).
- [38] R. Wiringa, R. Smith, and T. Ainsworth, Physical Review C **29**, 1207 (1984).
- [39] H. Kanada, T. Kaneko, S. Nagata, and M. Nomoto, Progress of Theoretical Physics **61**, 1327 (1979).
- [40] N. Itagaki, private communication.
- [41] N. Itagaki, K. Kobayakawa, and S. Aoyama, Physical Review C **68**, 054302 (2003).
- [42] R. Crespo and A. M. Moro, Physical Review C **76**, 054607 (2007).
- [43] P. K. Deb *et al.*, Physical Review Letter **86**, 3248 (2001).
- [44] S. Karataglidis *et al.*, Physical Review C **65**, 044306 (2002).
- [45] A. Lagoyannis *et al.*, Physics Letters B **518**, 27 (2001).
- [46] S. V. Stepantsov *et al.*, Physics Letters B **542**, 35 (2002).
- [47] H. Togawa and H. Sakaguchi, RCNP Annual Report 1 (1987).